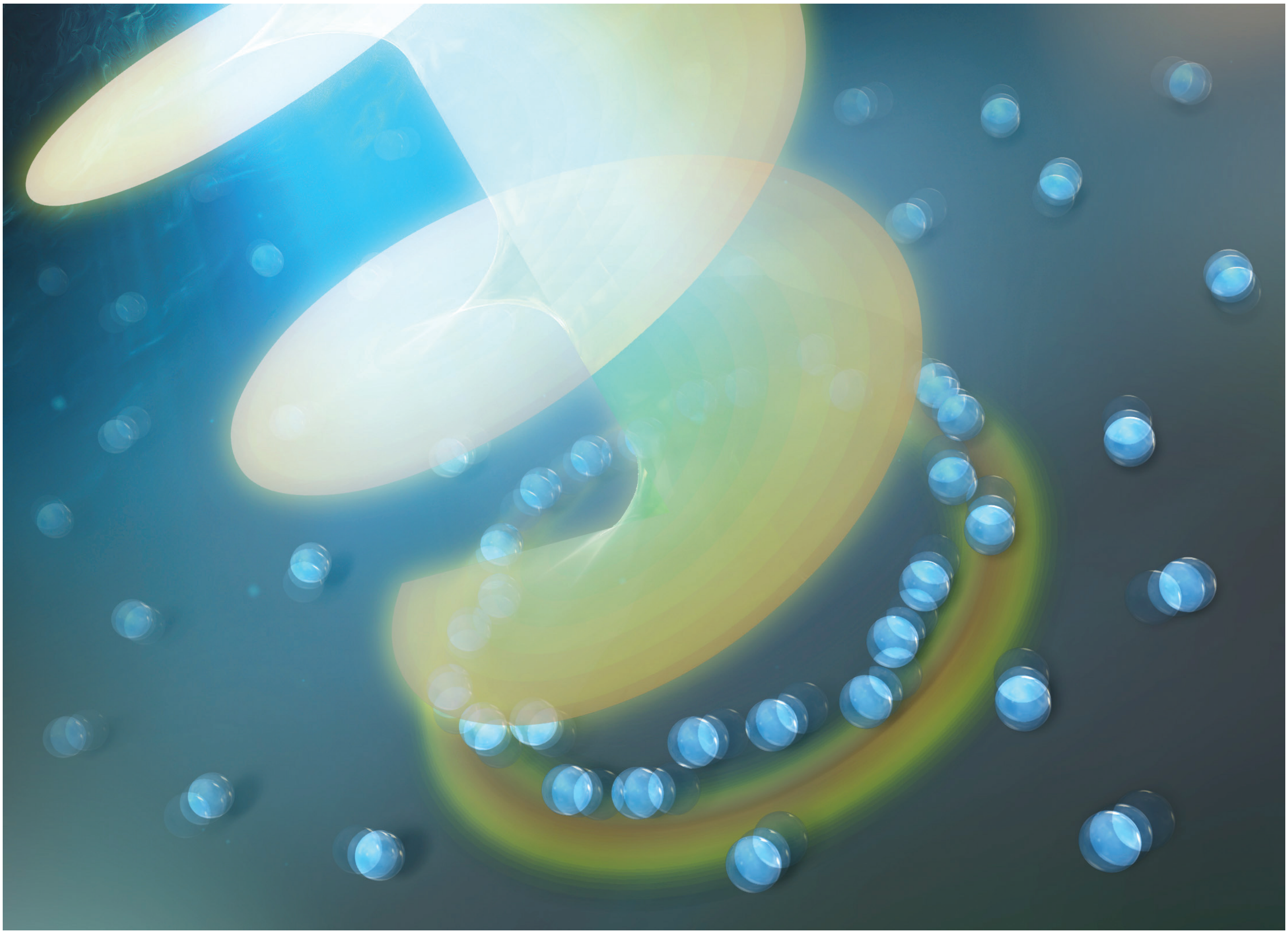

Showcasing research from the Graduate School of Engineering Science, Osaka University, Toyonaka, Japan.

Effect of hydrodynamic inter-particle interaction on the orbital motion of dielectric nanoparticles driven by an optical vortex

Nanoparticles in liquids can be trapped in the ring-like intensity distribution of an optical vortex and undergo two-dimensional orbital motion along the ring. It is reported both experimentally and theoretically that hydrodynamic inter-particle interaction between dielectric nanoparticles on the ring can accelerate their orbital speed. The present paper reveals the importance of hydrodynamic effect in optical manipulation even when the particles are nanoscale and Brownian, proposing the new aspect of particle manipulation by an optical vortex.

As featured in:

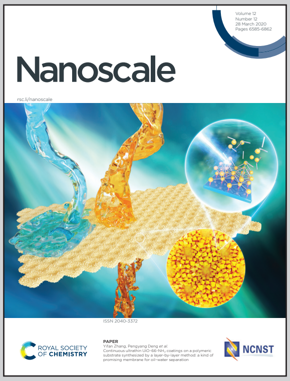

Volume 12
Number 12
28 March 2020
Pages 6585-6862

Nanoscale

rsc.li/nanoscale

ISSN 2040-3372

ROYAL SOCIETY OF CHEMISTRY

PAPER
Yifan Zhang, Pengyang Deng *et al.*
Continuous ultrathin UiO-66-NH_2 coatings on a polymeric substrate synthesized by a layer-by-layer method: a kind of promising membrane for oil–water separation

NCNST

See Tetsuro Tsuji, Satoyuki Kawano *et al.*, *Nanoscale*, 2020, **12**, 6673.

Nanoscale

PAPER

View Article Online
View Journal | View Issue

Check for updates

Cite this: *Nanoscale*, 2020, **12**, 6673

Effect of hydrodynamic inter-particle interaction on the orbital motion of dielectric nanoparticles driven by an optical vortex†

Tetsuro Tsuji, *‡ Ryoji Nakatsuka, Kichitaro Nakajima, Kentaro Doi and Satoyuki Kawano*

Received 15th December 2019,
Accepted 21st January 2020

DOI: 10.1039/c9nr10591c

rsc.li/nanoscale

We experimentally and theoretically characterize dielectric nano- and microparticle orbital motion induced by an optical vortex of the Laguerre–Gaussian beam. The key to stable orbiting of dielectric nanoparticles is hydrodynamic inter-particle interaction and microscale confinement of slit-like fluidic channels. As the number of particles in the orbit increases, the hydrodynamic inter-particle interaction accelerates orbital motion to overcome the inherent thermal fluctuation. The microscale confinement in the beam propagation direction helps to increase the number of trapped particles by reducing their probability of escape from the optical trap. The diameter of the orbit increases as the azimuthal mode of the optical vortex increases, but the orbital speed is shown to be insensitive to the azimuthal mode, provided that the number density of the particles in the orbit is same. We use experiments, simulation, and theory to quantify and compare the contributions of thermal fluctuation such as diffusion coefficients, optical forces, and hydrodynamic inter-particle interaction, and show that the hydrodynamic effect is significant for circumferential motion. The optical vortex beam with hydrodynamic inter-particle interaction and microscale confinement will contribute to biosciences and nanotechnology by aiding in developing new methods of manipulating dielectric and nanoscale biological samples in optical trapping communities.

Introduction

The optical vortex was proposed by Allen *et al.*[1–3] and had a ring-like transverse intensity distribution and optical angular momentum. This feature of the optical vortex drives the orbital motion of target particles along the ring-like intensity distribution, where the ring trapping and orbital motion are mainly caused by the optical gradient and scattering forces, respectively. Experiments have been done on the orbital motion of non-biological particles, especially latex beads with diameters of a few micrometers,[4–12] metal particles with diameters of several hundred nanometers to a few micrometers,[13–17] and glass or silica particles.[18,19] Some theoretical studies and modeling[20–23] have also been conducted. The theoretical studies[20,22] have involved multiple orbiting particles accelerated by hydrodynamic interaction between non-Brownian particles[20] and light-induced interaction between gold nanoparticles.[22] Plasmonic nanoparticles such as gold nanoparticles are relatively easy to manipulate optically because of their high polarizability. However, dielectric nanoparticles, which have low polarizability, have been rarely reported for a diameter less than one micrometer, because smaller particles are more difficult to stably trap in an orbit owing to the significant thermal fluctuation and weak optical forces. Because some target particles in biomedical applications (such as viruses[24,25]) are dielectric and have a characteristic length of several tens or hundreds of nanometers, manipulation of dielectric Brownian nanoparticles with an optical vortex should be explored for treating nanoscale biological samples. It should be noted that the optical vortex has been applied not only to the orbital motion of target particles but also to fabricating chiral nano-structures such as metal needles,[26,27] polymer needles,[28,29] and helical plastic fibers.[30] Therefore, developing technologies using the optical vortex will contribute to various research fields such as biosciences and nanofabrication.

Given such growing interest in the field, this paper addresses techniques for improving particle manipulation technologies and validates them both experimentally and theoretically. The novel aspect is that the technique is not based on optics but rather on mechanics. We systematically

---

Graduate School of Engineering Science, Osaka University, Toyonaka 560-8531, Japan. E-mail: tsuji.tetsuro.7x@kyoto-u.ac.jp, kawano@me.es.osaka-u.ac.jp

†Electronic supplementary information (ESI) available. See DOI: 10.1039/C9NR10591C

‡Present address: Graduate School of Informatics, Kyoto University, Kyoto 606–8501, Japan.

investigate the optical-vortex-induced motion of dielectric micro- and nanoparticles with diameters ranging from 0.2 μm to 2 μm, which includes biological scales from viruses to cells. The two key ideas for the successful optical manipulation of nanoparticles are hydrodynamic inter-particle interaction and microscale confinement of slit-like fluidic channels. We find that the number of particles trapped in an orbit is important in the dynamics of orbital motion: the orbiting speed increases with the number of nanoparticles. This acceleration is schematically described in Fig. 1 and the ESI (Movie S1†). A theoretical model including hydrodynamic interaction[8,10–12,20] explained the qualitative characteristics of microparticle motion observed in experiments. The diameter of the orbit increases as the azimuthal mode of the optical vortex increases, but the orbital speed is shown to be insensitive to the azimuthal mode, provided that the number density of the particles in the orbit is same. Such a trend is shown to be closely related to the above-mentioned hydrodynamic interaction. It should be noted that when a perfect vortex beam[31,32] is used, the diameter of the orbit is independent of the azimuthal mode, and the orbital speed increases linearly as the azimuthal mode increases. For the stable orbital motion of the smallest particle investigated in this paper, which has a diameter of 0.2 μm, hydrodynamic inter-particle interaction is required to accelerate its speed enough to overcome the inherent thermal fluctuation, which is significant for nanoscale targets. Evaluating the orbital motion of such tiny particles is facilitated by using microchannels with a small height, high-precision flow control, and a mixture of non-fluorescent and fluorescent particles. In particular, channels with a small height that confine the motion to two dimensions reduce the chance that nanoparticles will escape the optical trap in the beam propagation direction, leading to a larger number of orbiting particles and thus enhancing orbiting speed.

Micro- and nanofluidic devices can be used to analyze target biological nanoparticles and/or molecules dispersed in fluids.[33] Various methods to control target motion have been proposed to overcome the difficulties of controlling nanoscale targets.[34] Among them, optical forces have attracted much attention because they are a non-contact and feasible method available to researchers in various fields.[35–41] In fact, optical manipulation of tiny particles or biomolecules has been a fundamental tool in state-of-the-art nanoscience and bioengineering ever since the discovery of optical trapping by Ashkin.[42] The method proposed in this paper enhances the controllability of nanoscale dielectric targets and contributes to the development of micro- and nanofluidic devices. Optical manipulation, electrophoresis,[43] and thermophoresis[44–46] are useful transport phenomena in tiny devices and have different physical mechanisms, so combining them will yield a selective manipulation method.[47,48]

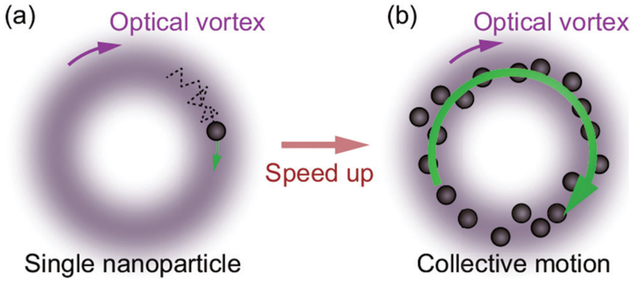

Fig. 1 Concept of orbiting acceleration due to hydrodynamic inter-particle interaction. (a) It is difficult to manipulate a single dielectric nanoparticle because of the weak optical force and inherent thermal fluctuation. However, when the number of particles in the orbit increases, as shown in panel (b), the collective nanoparticle motion leads to faster orbital speed that overcomes the thermal fluctuation.

Experimental methods

Optical setup

An overview of the experimental setup is shown in Fig. 2. First, an observation system is introduced. A microfluidic device is mounted on an inverted microscope (IX-71, Olympus, Tokyo, Japan). The details of the device will be explained later. An objective lens (OL) with a magnification of 20× (numerical aperture (NA) = 0.45, LCPLN20XIR, Olympus, Tokyo, Japan) or 50× (NA = 0.65, LCPLN50XIR, Olympus, Tokyo, Japan) is used to observe the particle motion in the device. Our sample solution is contained in a microchannel with a height $h \approx 3$ μm. Therefore, a high NA such as that of an oil immersion lens, which is frequently used in optical trapping, is not necessary because confinement prevents the target particles from being pushed out in the direction of beam propagation, resulting in stable trapping. An excitation light (Cobolt 06-MLD, Cobolt AB, Solna, Sweden) with a wavelength of 488 nm for fluorescence observation irradiates the device through the same OL. Fluorescence from a sample, which is a polystyrene particle described in Table 1, is monitored with a complementary-metal–oxide–semiconductor (CMOS) camera (Zyla 5.5, Andor Technology, Belfast, Northern Ireland) and analyzed with a personal computer (PC). A transmission light source (TLS) may be also used to observe non-fluorescent samples.

The wavelength of the laser used in this study is 1064 nm, because this wavelength is standard and frequently used in biosciences owing to the low absorption rate of the laser beam by water solutions. The optical vortex in our experiments is the Laguerre–Gaussian (LG) beam, which is one of the higher-order modes of a Gaussian beam. The LG beam is obtained by converting a continuous-wave (CW) Gaussian beam with a wavelength of 1064 nm (ASF1JE01, Fitel, Furukawa Electronics, Tokyo, Japan) using a liquid-crystal-on-silicon spatial-light-modulator (LCOS-SLM; X13138-03, Hamamatsu Photonics K.K., Hamamatsu, Japan), as shown in Fig. 2. More specifically, the PC sends a digital-visual-interface (DVI) signal to the LCOS-SLM to show a specific image on the LCOS-SLM display. If the Gaussian beam irradiates the display, the image produces a spatially inhomogeneous phase difference from the incident beam, and then the reflected beam becomes the optical vortex. The azimuthal mode m of the optical vortex may

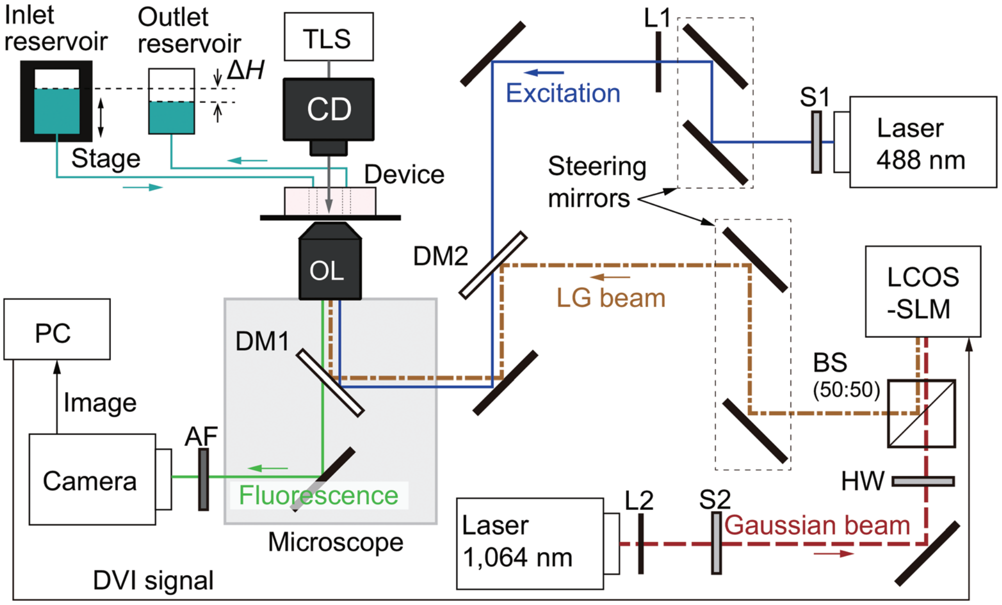

Fig. 2 Schematic of the experimental setup. AF: absorption filter to cut the laser with a wavelength of 1064 nm. BS: beam splitter. CD: condenser. DM1 and DM2: dichroic mirrors. DVI: digital visual interface. HW: half-wave plate to adjust the direction of linear polarization to that required by the liquid-crystal-on-silicon spatial-light-modulator (LCOS-SLM). L1 and L2: plano-convex lenses to obtain desired beam diameters. OL: objective lens. PC: personal computer. S1 and S2: shutters. TLS: transmission light source. The inlet and outlet reservoirs are used to control the channel flow rate. The photograph of the microfluidic device on the microscope stage is presented in Fig. S1.†

Table 1 Product names and concentrations of polystyrene particles for the samples with d_p = 0.2, 0.5, 1.0, and 2.0 μm

	Fluorescent particle (Molecular Probes, Eugene, USA)		Non-fluorescent particle (Merck, Darmstadt, Germany)	
d (μm)	Product name	Concentration	Product name	Concentration
0.2	F8811	2.0×10^{-4} wt%	K1-020	2.0×10^{-2} wt%
0.5	F8813	2.0×10^{-4} wt%	K1-050	1.5×10^{-2} wt%
1.0	F8823	2.0×10^{-4} wt%	K100	1.0×10^{-2} wt%
2.0	F8827	2.0×10^{-4} wt%	L200	1.0×10^{-2} wt%

be changed using another specific image. Before the Gaussian beam impinges on the LCOS-SLM, the direction of linear polarization of the beam must be modulated using a half-wave (HW) plate such that it is consistent with the LCOS-SLM specification. The LG beam is combined with the excitation light and introduced in the microscope. The optical power P_{laser} is measured at the top of the OL using a power meter (3A-QUAD, Ophir Optronics, Jerusalem, Israel).

Microfluidic device

The microfluidic device consists of a block of polydimethylsiloxane (PDMS; Sylgard®184, Dow Corning Toray Co., Tokyo, Japan) with a microchannel pattern and a cover glass (24 × 36 mm^2, no. 1, Matsunami Glass Co., Osaka, Japan). First, a silicon mold that has the microchannel pattern is fabricated as described in Appendix A. Then, PDMS is poured on the mold and cured. Removing the cured PDMS from the mold results in a PDMS block with the microchannel pattern. The microchannel height is determined by the height of the silicon mold, which is measured as h = 3.2 ± 0.1 μm using a laser scanning microscope (OLS4100, Olympus, Tokyo, Japan). Then, two holes for the inlet and outlet are fabricated in the PDMS block using a biopsy punch (2.0 mm in diameter, BP-25F, Kai Industries Co., Seki, Japan). Finally, after cleaning the contact surfaces of the PDMS block and the cover glass with a corona treater (BD-20AC, Electro-Technic Products, Chicago, USA), we bond them together to form the microfluidic device.

The microchannel pattern is schematically shown in Fig. 3(a). The channel height in the z direction is denoted by h,

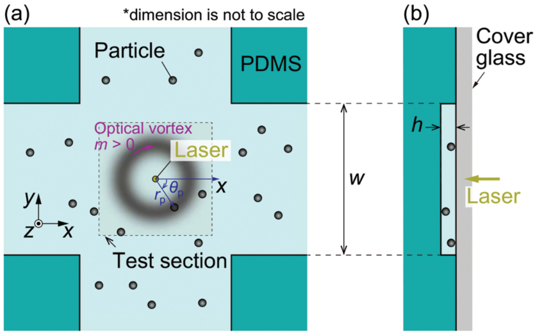

Fig. 3 Schematic of the microfluidic device. (a) Microscopic view from the bottom of the device. PDMS rectangular columns are fabricated with an interval w to avoid channel collapse. (b) Side view of the channel in the yz-plane.

as shown in the side view of Fig. 3(b). The center of the irradiated optical vortex is at the center of the test section. The radial coordinate of the particle is expressed as (r_p, θ_p), as shown in Fig. 3. The azimuthal mode m of the optical vortex is defined so that $d\theta_p/dt > 0$ when $m > 0$, where t is a time variable. The PDMS roof may collapse owing to the small microchannel height. To avoid collapse, square columns with an area of 100 × 100 μm^2 are fabricated in the channel with a spatial interval of w = 100 μm in both the x and y directions.

Sample particles

The sample solution contains a mixture of fluorescent and non-fluorescent polystyrene (PS) particles with the same diameter d_p. The product name and bead concentrations are listed in Table 1. For instance, for d_p = 0.2 μm, the sample solution is prepared by diluting the stock solutions of the fluorescent particles (F8811) and non-fluorescent particles (K1-020) using the non-ionic surfactant solvent Triton X-100 (1 wt%). The surfactant is necessary to avoid the sticking of particles to the channel walls because our sample solution is confined to a narrow space where the particles have frequent chances to contact the wall.

The reason for using a mixture of 2.0×10^{-4} wt% dilute fluorescent particles and $\leq 2.0 \times 10^{-2}$ wt% dense non-fluorescent particles is to facilitate particle tracking (see Movie S1†). We optically trap both types of particles in the circular path so that a single fluorescent particle is contained. In this way, only the fluorescent particle is recognized in the particle tracking algorithm. Using such a mixture of fluorescent and non-fluorescent particles is especially important when d_p is small and the number of particles in the circular path, N, is large. For the particle tracking from the obtained video images, we use an image analysis software ImageJ and its plugin Particle Track and Analysis (PTA).

Experimental procedure

All the experiments were carried out at the room temperature of 297.7 ± 1.7 K. The fluid flow in the channel should be kept negligibly small to eliminate the biased drag force acting on the particles. The fluid flow is controlled as follows. The PDMS block has an inlet hole with a diameter of 2 mm. A silicone tube connects the inlet hole to the inlet reservoir, as shown in Fig. 2. The same tube connection is also made to the outlet hole of the PDMS and the outlet reservoir. The sample solution is poured into the reservoirs, and the whole device and reservoirs are deaerated in a vacuum chamber to remove remaining bubbles in the microchannel. After the deaeration, there is an inherent water-level difference ΔH between the inlet and outlet reservoirs that induces the mean flow in the microchannel, as shown in Fig. 2. Because the unwanted mean flow can affect the analysis of particle motion induced by the optical vortex, the water-level difference ΔH is set to be zero using an automatic stage (SGSP20-35, Sigma Koki, Japan) with a precision of $\Delta H_{\min}$ = 1 μm. Note that the pressure difference ΔP between the inlet and outlet reservoirs can be controlled with a high resolution $\Delta P = \rho g \Delta H_{\min} \approx 0.01$ Pa, where $\rho = 1.0 \times 10^3$ kg m^{-3} is the fluid density and g = 9.8 m s^{-2} is the acceleration of gravity. The complete absence of mean flow can be verified by checking the video of the PS particles. In fact, using the particle tracking velocimetry, the magnitude of mean flow is estimated as 0.2 μm s^{-1} at most. Then, the sample solution confined in the slit-like microchannel is irradiated by the focused LG beam in the perpendicular direction, as shown in Fig. 3.

Theoretical model

Micro- and nanofluid dynamics

In this section, we introduce a model based on the literature[8,10–12,20] that accounts for hydrodynamic inter-particle interaction. These references modeled optical forces as simple heuristic functions and did not consider thermal fluctuation. The effect of thermal fluctuation may be negligible for particles with diameters larger than 2 μm in water (*e.g.*, ref. 8 uses a particle with a diameter of 3 μm and the theoretical model without thermal fluctuation well predicted the experimental results), but it is significant for particles with a diameter of 0.2 μm. This paper uses a more realistic model of optical forces and includes the effect of thermal fluctuation to simulate particles with a diameter of 0.2 μm.

We consider the two-dimensional motion of N particles with mass m_p and radius $a_p = d_p/2$ in the focal plane, which is the xy plane of the Cartesian coordinate system as shown in Fig. 3. The motion is induced by an optical vortex. The position and velocity of the nth particle (n = 1, …, N) are denoted by $\boldsymbol{r}_n(t) = (x_n(t), y_n(t))$ and $\boldsymbol{v}_n(t) = (v_{x,n}(t), v_{y,n}(t))$. We also introduce the polar coordinates $(x,y) = (r\cos\theta, r\sin\theta)$. The unit vectors in the r and θ directions are $\boldsymbol{e}_{n,r} = (x_n/r, y_n/r)$ and $\boldsymbol{e}_{n,\theta} = (-y_n/r, x_n/r)$, respectively. The circumferential component of the particle velocity is then written as $v_{n,\theta} = \boldsymbol{v}_n \cdot \boldsymbol{e}_{n,\theta}$. The Reynolds number Re is a non-dimensional parameter in fluid mechanics that is the ratio of inertial to viscous effects. In this setting, we have $\mathrm{Re} \equiv \rho(d_p/2)v_{n,\theta}/\eta = 5.8 \times 10^{-7}$ for representative values $v_{n,\theta}$ = 1 μm s^{-1} and d_p = 1 μm, where the viscosity of water is $\eta = 8.55 \times 10^{-4}$ Pa s at 300 K. The value of 300 K is slightly larger than that in the experiment, 297.7 K. The relative difference is less than 0.8% and we do not think the results are affected by this difference. Because $\mathrm{Re} \ll 1$, we can safely neglect the inertial effect and assume Stokes drag acts on the particle. However, we need additional justification for applying Stokes drag to this problem because the sphere is orbiting around the origin with a radius r_{trap}; that is, the sphere experiences an effective shear flow and not a uniform flow in which the Stokes drag is justified. We discuss this point in Appendix B and describe the Stokes dynamics next.

The characteristic time scale τ of the motion is given by $\tau = m_p/(6\pi a_p \eta)$ = 68 ns for a_p = 0.5 μm, and is much smaller than the time scales of the simulation and experiment in the aqueous solution of this study. Therefore, we can neglect the inertial term of the equation of motion. The motion of the nth particle is hydrodynamically affected by that of the others, which have the index $n' \neq n$, and thus the over-damped equations are written as

$$\frac{\partial \boldsymbol{r}_n}{\partial t} = \boldsymbol{v}_n(t), \quad \boldsymbol{r}_n(0) = \boldsymbol{r}_n^0, \tag{1a}$$

$$\begin{aligned} \boldsymbol{v}_n(t) &= \tilde{\mu}_{nn}\boldsymbol{f}_n + \tilde{\mu}_{nn}\boldsymbol{f}_n^{\mathrm{hydr}}, \\ \tilde{\mu}_{nn}\boldsymbol{f}_n^{\mathrm{hydr}} &= \sum_{n' \neq n} \tilde{\mu}_{nn}\boldsymbol{f}_{n'}, \quad \boldsymbol{v}_n(0) = \boldsymbol{v}_n^0. \end{aligned} \tag{1b}$$

Here, the index n' in $\sum_{n' \neq n}$ takes on the values 1, …, $n - 1$, $n + 1$, …, N; $\boldsymbol{f}_n = (f_{x,n}, f_{y,n})$ is the force acting on the nth particle other than the drag; $\boldsymbol{r}_n^0$ and $\boldsymbol{v}_n^0$ are the initial position and velocity, respectively; and $\tilde{\mu}_{nn'}$ is a tensor defined as

$$\tilde{\mu}_{nn'} = \frac{1}{6\pi\eta a_{\mathrm{p}}}\mathcal{I}, \quad (n = n'), \tag{2a}$$

$$\begin{aligned} \tilde{\mu}_{nn'}(\boldsymbol{r}_{nn'}) = {} & \frac{1}{8\pi\eta|\boldsymbol{r}_{nn'}|}\left(\mathcal{I} + \frac{\boldsymbol{r}_{nn'} \otimes \boldsymbol{r}_{nn'}}{|\boldsymbol{r}_{nn'}|^2}\right) \\ & + \frac{{a_{\mathrm{p}}}^2}{12\pi\eta|\boldsymbol{r}_{nn'}|^3}\left(\mathcal{I} - \frac{3\boldsymbol{r}_{nn'} \otimes \boldsymbol{r}_{nn'}}{|\boldsymbol{r}_{nn'}|^2}\right), \quad (n \neq n'), \end{aligned} \tag{2b}$$

$$\boldsymbol{r}_{nn'}(t) = \boldsymbol{r}_n - \boldsymbol{r}_{n'}, \tag{2c}$$

where $\tilde{\mu}_{nn'}$ is related to the Rotne–Prager–Yamakawa mobility tensor[8,10–12,20,49,50] $\mu_{nn'}$ as $\mu_{nn'} = (6\pi a_{\mathrm{p}}\eta)\tilde{\mu}_{nn'}$. The operation $\otimes$ is a tensor product, $\boldsymbol{f}_n^{\mathrm{hydr}}$ is the hydrodynamic inter-particle interaction, and $\mathcal{I}$ is the identity matrix. We focus on the circumferential component by taking the dot product of $\boldsymbol{e}_{n,\theta}$ and eqn (1b); that is, we define f_θ and v_θ as:

$$\begin{aligned} f_\theta &= 6\pi a_{\mathrm{p}}\eta v_\theta \\ &= \frac{1}{N}\sum_{n=1}^{N}\left[6\pi a_{\mathrm{p}}\eta(\tilde{\mu}_{nn}\boldsymbol{f}_n + \tilde{\mu}_{nn}\boldsymbol{f}_n^{\mathrm{hydr}}) \cdot \boldsymbol{e}_{n,\theta}\right], \end{aligned} \tag{3}$$

which is an averaged effective Stokes drag. This study analyzes the motion of a target particle experimentally and obtains its circumferential velocity v_θ in the orbital motion. It is useful to estimate the magnitude of the force f_θ acting on the particle for application to microfluidic devices, where other forces such as electrophoretic, dielectrophoretic, thermophoretic, random, and drag forces may be comparable to the optical force. Note that if we neglect the hydrodynamic inter-particle interaction $\boldsymbol{f}_n^{\mathrm{hydr}}$ by setting $N = 1$, we find that the Stokes drag $6\pi\eta a_{\mathrm{p}}v_\theta$ is balanced by the external force f_θ.

The force $\boldsymbol{f}_n$ is the superposition of the optical scattering force $\boldsymbol{f}^{\mathrm{scat}}$,[51] the gradient force $\boldsymbol{f}^{\mathrm{grad}}$,[52] the short-range repulsive force between particles $\boldsymbol{f}^{\mathrm{rep}}$,[20] and the thermal fluctuation $\boldsymbol{f}^{\mathrm{rand}}$:

$$\begin{aligned} \boldsymbol{f}_n(t) = {} & \boldsymbol{f}^{\mathrm{scat}}(\boldsymbol{r}_n(t)) + \boldsymbol{f}^{\mathrm{grad}}(\boldsymbol{r}_n(t)) \\ & + \sum_{n' \neq n} f^{\mathrm{rep}}(\boldsymbol{r}_{nn'}(t)) + f^{\mathrm{rand}}, \end{aligned} \tag{4a}$$

$$\boldsymbol{f}^{\mathrm{scat}}(\boldsymbol{r}_n) = S_c p_0 \sigma^2 F_m(|\boldsymbol{r}_n|)\frac{m}{k|\boldsymbol{r}_n|}\boldsymbol{e}_{n,\theta}, \tag{4b}$$

$$\boldsymbol{f}^{\mathrm{grad}}(\boldsymbol{r}_n) = p_0 \alpha_V F_m(|\boldsymbol{r}_n|)\left(\frac{2|m|}{|\boldsymbol{r}_n|} - \frac{4|\boldsymbol{r}_n|}{{w_0}^2}\right)\boldsymbol{e}_{n,r}, \tag{4c}$$

$$\boldsymbol{f}^{\mathrm{rep}}(\boldsymbol{r}_{nn'}) = E_0^{\mathrm{rep}}\frac{\partial}{\partial \boldsymbol{r}_{nn'}}\left(\left(\frac{|r_{nn'}|}{2a_{\mathrm{p}}}\right)^{12} - 1\right)^{-1}, \tag{4d}$$

$$\langle \boldsymbol{f}^{\mathrm{rand}}(t)\rangle = 0, \quad \langle \boldsymbol{f}^{\mathrm{rand}}(t_1) \otimes \boldsymbol{f}^{\mathrm{rand}}(t_2)\rangle = 2\mathcal{I}\xi k_{\mathrm{B}}T\delta(t_1 - t_2), \tag{4e}$$

where $p_0 = {n_{\mathrm{f}}}^2\varepsilon_0{E_0}^2/2$ [Pa] is the reference optical pressure, $\alpha_{\mathrm{V}} = 2\pi{a_{\mathrm{p}}}^3({n_{\mathrm{p}}}^2 - {n_{\mathrm{f}}}^2)/({n_{\mathrm{p}}}^2 + 2{n_{\mathrm{f}}}^2)$ [m^3] is the polarizability volume, and

$$\begin{aligned} & k = 2\pi n_{\mathrm{f}}/\lambda, \quad F_m(r) = \frac{2}{\pi|m|!}\left(\frac{\sqrt{2}r}{w_0}\right)^{2|m|}\exp\left(-\frac{2r^2}{{w_0}^2}\right), \\ & \xi = 6\pi a_{\mathrm{p}}\eta. \end{aligned} \tag{5}$$

The quantity $\langle x\rangle$ is the ensemble average of x, $\delta(x)$ is the delta function, w_0 is the radius of the beam waist at the focal plane, $k_{\mathrm{B}} = 1.38 \times 10^{-23}$ m^2 kg s^{-2} K^{-1} is the Boltzmann constant, ξ is the friction coefficient, $T = 300$ K is the temperature of water, σ^2 is the scattering cross section, $n_{\mathrm{f}} = 1.333$ and $n_{\mathrm{p}} = 1.592$ are the refractive indices of the fluid and particle, $\varepsilon_0 = 8.85 \times 10^{-12}$ F m^{-1} is the dielectric constant, E_0 is the magnitude of the electric field, $E_0^{\mathrm{rep}} = 2.00 \times 10^{-21}$ J is the magnitude of the repulsive potential, and S_{c} in eqn (4b) is a constant smaller than unity. We introduce S_{c} because the model may overestimate the scattering force when the condition $d \ll \lambda$ is not satisfied, as reported for Rayleigh theory.[52] We determine E_0^{rep} such that particles never overlap during the simulation. The laser power is

$$P_{\mathrm{laser}} = (n_{\mathrm{f}}c\varepsilon_0/4)(\pi{w_0}^2){E_0}^2, \tag{6}$$

where $c = 3.00 \times 10^8$ m s^{-1} is the speed of light. We can use the experimental values of w_0 and P_{laser}. The scattering cross section is obtained from Mie theory as $\sigma^2 = 8.53 \times 10^{-1}$ μm^2 for $d_{\mathrm{p}} = 1$ μm and $\sigma^2 = 4.31 \times 10^{-4}$ μm^2 for $d_{\mathrm{p}} = 0.2$ μm. The gradient force in eqn (4c) is based on the Rayleigh approximation, which is applicable for particle diameters much smaller than the wavelength of the incident laser beam. Therefore, a particle with $d_{\mathrm{p}} = 1$ μm is out of the range of application. Nonetheless, Rayleigh theory well predicts the gradient force for particles out of this diameter range.[52]

The above equations are used to investigate the effect of the number of particles N on the particle dynamics, especially the average angular frequency $\omega = \frac{1}{N}\sum_{n=1}^{N}\frac{1}{(t_1 - t_0)}\int_{t_0}^{t_1}\boldsymbol{v}_n \cdot \boldsymbol{e}_{n,\theta}/|\boldsymbol{r}_n|\mathrm{d}t$, where $t_0 = 1$ s and $t_1 = 10$ s determine the sampling interval in the simulation. The effect of the initial configuration disappears for $t > 1$ s. The time step of the simulation is taken to be $\Delta t = 1 \times 10^{-7}$ s, and Δt is small enough to avoid Δt-dependence of the results.

Analytical remarks on the orbital motion

Target particles are confined in the orbit by the optical gradient force $\boldsymbol{f}^{\mathrm{grad}}$ in the radial direction as described by eqn (4c). The particles are trapped at the radial position $r_{\mathrm{trap}}^{(m)}$ such that $\boldsymbol{e}_{n,r}\cdot\boldsymbol{f}^{\mathrm{grad}}(r_{\mathrm{trap}}^{(m)}) = 0$, that is, $r_{\mathrm{trap}}^{(m)} = w_0\sqrt{m/2}$. To eliminate the dependence on w_0 for qualitative discussion, we focus on the radius change rate defined as

$$r_{\mathrm{ratio}} \equiv \frac{r_{\mathrm{trap}}^{(m)}}{r_{\mathrm{trap}}^{(m-1)}} = \sqrt{\frac{m}{m-1}}. \tag{7}$$

The rate r_{ratio} will be used to validate the experimental results.

We remark that the scattering force $\boldsymbol{f}^{\mathrm{scat}}(\boldsymbol{r}_n)$ with $|\boldsymbol{r}_n| = r_{\mathrm{trap}}^{(m)}$ acts on the particles trapped in the orbit. Substituting $|\boldsymbol{r}_n| = r_{\mathrm{trap}}^{(m)} = w_0\sqrt{m/2}$ in eqn (4b), we obtain $|\boldsymbol{f}^{\mathrm{scat}}| = C_0A(m)$, where C_0 is a constant independent of m and $A(m) = (m^m/m!)\exp(-m)\sqrt{m}$. We can check that $A(m)$ is a monotonically increasing function with respect to m and $\lim_{m\to\infty} A(m)/A(1) \approx 1.084$; that is, $|\boldsymbol{f}^{\mathrm{scat}}|$ can be considered to be almost independent from m:

$$|\boldsymbol{f}^{\mathrm{scat}}| \approx C_0A(1), \quad (C_0:\ \text{independent from } m). \tag{8}$$

This observation is important because eqn (8) indicates that m does not affect the orbital speed. However, the gradient force depends on the azimuthal mode m. To see this, consider that the particles are trapped near the equilibrium position, meaning $|\boldsymbol{r}_n| \approx r_{\mathrm{trap}}^{(m)}$, as shown in Fig. 6. We introduce the trapping stiffness $K = -\partial|\boldsymbol{f}^{\mathrm{grad}}|/\partial|\boldsymbol{r}_n|$ at $|\boldsymbol{r}_n| = r_{\mathrm{trap}}^{(m)}$, which corresponds to a "spring constant" in the radial direction. Then, it is seen that $|K| = C_1(m^m/m!)\exp(-m)$, where C_1 is a constant independent of m. Since $\tilde{K}(m) \equiv |K|/C_1$ is a monotonically decreasing function of m, *e.g.*, $\tilde{K}(1) = 0.368$, $\tilde{K}(2) = 0.271$, $\tilde{K}(3) = 0.224$, $\tilde{K}(4) = 0.195$; $\tilde{K}(m)(= A(m)/\sqrt{m}) = 0.399 \times m^{-1/2}$ for $m \gg 1$, the optical trapping in the radial direction by the gradient force becomes weaker as m increases.

Results and discussion

Orbital motion of nano- and microparticles

This section presents an overview of the orbital motion of nano- and microparticles with d_{p} = 0.2, 0.5, 1.0, and 2.0 μm in the test section, as shown in Fig. 3. As will be more closely investigated later, the orbital speed depends on the number of particles N trapped in the orbit. However, it is difficult to count the particles *in situ* when d_{p} = 0.2 and 0.5 μm owing to their small size and strong thermal fluctuation. Therefore, the results in this section for d_{p} = 0.2 and 0.5 μm are all for a saturated state, in which the entire orbit is occupied by many particles, and for these cases the nanoparticles may not form a single necklace that is seen in Movie S1† for d_{p} = 1 μm. Recall that, in our experiments, the orbit includes a single fluorescent particle and many other non-fluorescent particles, where the fluorescent one is tracked. The fluorescent particle is treated as the representative, and the experimental result of the tracking will be compared with the ensemble average of the simulation results. The OL magnification is 50× for d_{p} = 0.2 μm and 20× for the other cases.

Before going into detail, we remark on the θ_{p}-dependence of the dynamics observed in the experiment. The created LG beam intensity has slight inhomogeneity in the azimuthal direction, that is, the imperfection of the optical vortex seems to exist in our experiment. This can be seen from Movie S1:† the orbital speed for the case of N = 8 in the movie seems to be not constant during a single orbiting, *i.e.*, the speed is higher when $\theta_{\mathrm{p}} \approx \pi/2$ than when $\theta_{\mathrm{p}} \approx 3\pi/2$, where the definition of θ_{p} is found in Fig. 3(a). However, the effect of θ_{p}-dependence can be reduced by considering the time-averaged angular frequency, as discussed in Appendix C with more detailed data analysis on the dynamics during the orbital motion. Therefore, we mainly discuss in this paper the time-averaged orbital speed.

Fig. 4 shows the snapshots of the orbital motion of nano- and microparticles with diameters of 0.2, 0.5, 1.0, and 2.0 μm, using an optical vortex with m = 1. Note that the length of the scale bar is different for d_{p} = 0.2 μm. As shown in Fig. 2, only the excitation light of wavelength 488 nm is used for d_{p} = 0.2 and 0.5 μm, while both the excitation and transmission lights are used for d_p = 1.0 and 2.0 μm. The absence of the transmission light for d_{p} = 0.2 and 0.5 μm is to increase the signal-to-noise ratio of the fluorescence intensity of the tracked particle, where the fluorescent particle can only be detected. We see that the particle with d_{p} = 0.2 μm does about half a revolution in 0.40 s, while the particles with d_{p} = 0.5 and 1.0 μm do about one revolution in 0.40 s. The particle with d_{p} = 2.0 μm is the fastest and completes about one and a half revolutions in 0.20 s. In the ESI (Movie S2†), we show that the particle cannot undergo the orbital motion without the microscale confinement.

Next, we investigate the orbital characteristics more systematically. The particle tracking is carried out using a video with 50 fps. This frame rate is considered enough to analyze orbital motion with a frequency of $O(1)$ Hz, which is typical of the experimental conditions of this study. To further validate the frame rate, we compare the orbital frequencies obtained with 50 fps and 1000 fps for d_{p} = 0.2 μm, where the thermal fluctuation is the most significant among the cases investigated here. Fig. 5 shows the radial and circumferential positions r_{p} and θ_{p} as a function of time for a laser power P_{laser} = 313 mW and azimuthal mode m = 1. The linear-fit curves agree very well for 50 fps and 1000 fps. The rotational frequency ω, which is the slope of the linear fits, is computed for both cases to compare them quantitatively. We obtain $\omega = 2.68 \times 10^{-1}$ Hz for both 50 fps and 1000 fps, and the deviation is less than 0.4%. For the radial direction, the difference in variance σ_{r}^2 of the resulting position distribution for 50 Hz and 1000 Hz is less than 4%. Therefore, we conclude that a frame rate of 50 fps is enough to analyze orbital motion with thermal fluctuation.

In the following, the azimuthal mode is set to be m = 1 for d_{p} = 0.2 μm and m = 1, 3, 5, and 7 for $d_{\mathrm{p}} \geq 0.5$ μm. It is difficult for our experimental apparatus to trap a particle with

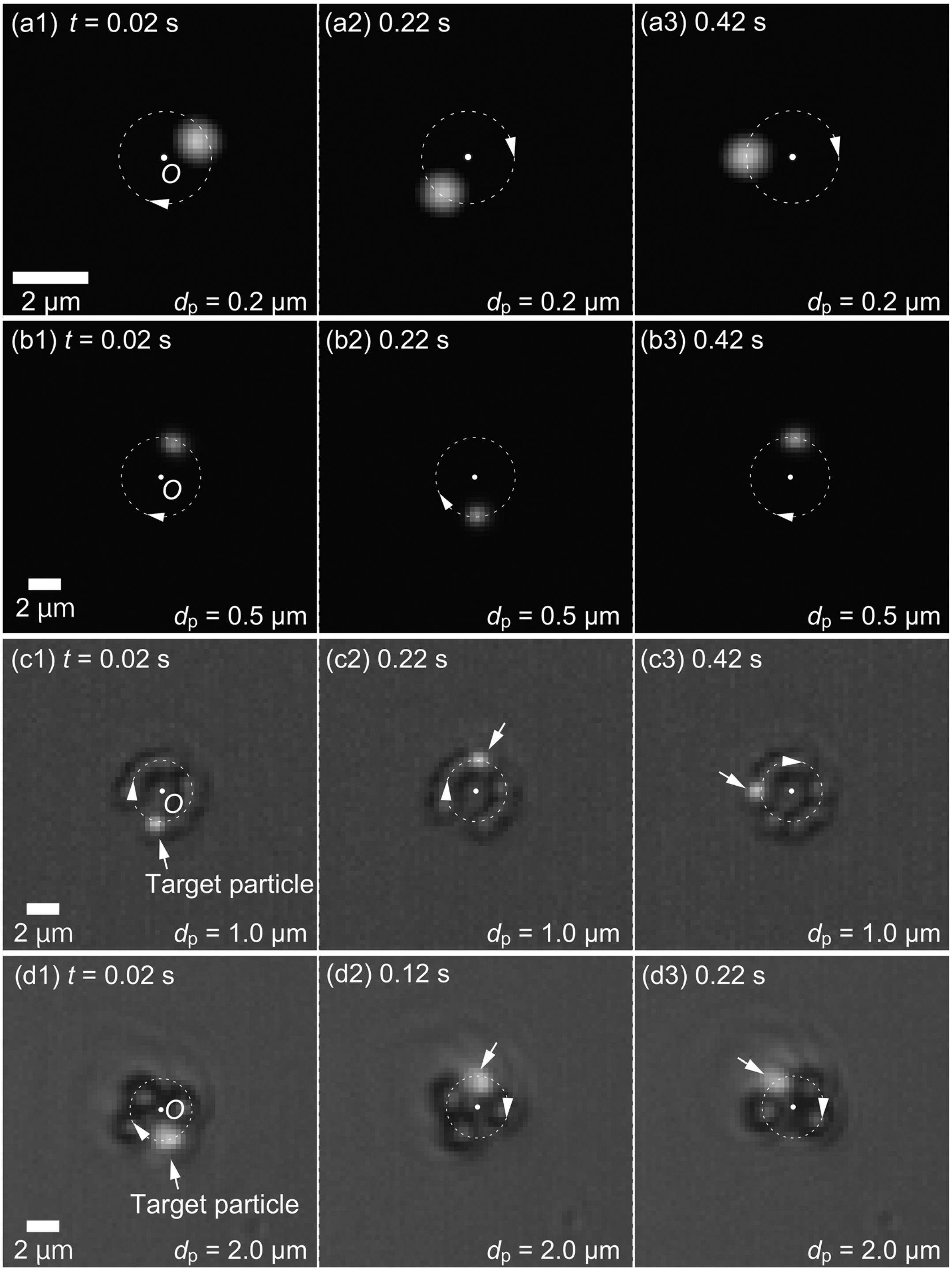

Fig. 4 Snapshots of orbital motion of nano- and microparticles with diameters of (a1)–(a3) 0.2, (b1)–(b3) 0.5, (c1)–(c3) 1.0, and (d1)–(d3) 2.0 μm. The optical vortex with the azimuthal mode $m = 1$ is used. The laser power P_{laser} is (a1)–(a3) $P_{\text{laser}} = 408$, (b1)–(b3) 554, (c1)–(c3) 541, and (d1)–(d3) 532 mW. For $d_{\text{p}} = 0.2$ and 0.5 μm, the transmission light is not used so that we can focus on the motion of a fluorescent particle. Note that the orbits are occupied by invisible non-fluorescent particles. For $d_{\text{p}} = 1.0$ and 2.0 μm, the transmission light for microscopy is also used, and we see that the orbit is occupied by a single fluorescent and multiple non-fluorescent particles. The signal-to-noise ratio is high enough to track the single fluorescent particle for $d_{\text{p}} = 1.0$ and 2.0 μm even under the transmission light.

$d_{\text{p}} = 0.2$ μm and $m \geq 2$ because of the strong thermal fluctuation and weak optical gradient force. Stronger thermal fluctuation for smaller d_{p} can be seen theoretically from eqn (4e), which leads to the situation that the contribution of the random force to the velocity, $\tilde{\mu}_{nn}\boldsymbol{f}^{\text{rand}}$, is proportional to $a_{\text{p}}{}^{-1/2}$. A weaker optical gradient force for a smaller d_{p} is theoretically predicted

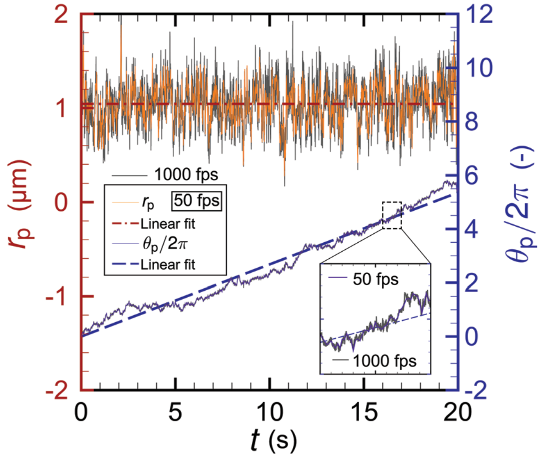

Fig. 5 Radial and circumferential positions r_p and θ_p of a trapped particle with d_p = 0.2 μm as a function of time. The laser power is set to be 313 mW and the azimuthal mode to m = 1. The straight lines are the fits to the raw data. The data for 1000 fps are shown with gray lines. The effect of the frame rate used in analyzing orbital motion is not significant because two data for 50 fps and 1000 fps agree with a deviation less than 0.4%.

as discussed previously below eqn (8). Therefore, the results for d_p = 0.2 and $d_p \geq 0.5$ μm are next presented separately.

(i) Case of d_p = 0.2 μm

Fig. 6 shows the result of particle tracking for d_p = 0.2 μm and $P_{\rm laser}$ = (a) 408, (b) 367, (c) 313, (d) 295, (e) 223, and (f) 148 mW. The left (red) axis is the distance r_p from the beam center and the right (blue) axis the circumferential coordinate θ_p. The particles undergo thermal fluctuation near an equilibrium position around $r_p \approx 1$ μm. Note that we are considering a Brownian particle under an external optical force, and thus its motion is different from ordinary diffusion in a free solution, where the diffusion coefficient D can be described as $D = \sigma_r^2/(2t)$. The data for $P_{\rm laser}$ = 223 and 148 mW in Fig. 6(e) and (f), respectively, terminate at $t \approx 18$ s and 5 s because the trapped particles escape at these times owing to insufficient optical power to overcome the thermal fluctuation. We see from the figure that r_p is fluctuating but constant on average in time, and θ_p linearly increases with time as long as the particle is trapped. Therefore, we treat r_p as the radius $r_{\rm trap}$ of the orbit of trapped particles. The details of the radial force balance will be discussed in the next paragraph. We conclude that the nanoparticle with the diameter of 0.2 μm, which is much smaller than that previously reported,[4–12] is driven to stable orbital motion by the optical vortex. The angular frequency for $P_{\rm laser}$ = 408 mW is ω = 3.31 rad s^{-1}. This success of nanoparticle optical trapping and orbiting is due to the hydrodynamic inter-particle interaction, as will be described later with the simulation results. Fig. 6(g) shows the circumferential force f_θ, obtained using eqn (3), acting on the particles for various laser powers. If the optical force is sufficiently larger than the magnitude of the thermal fluctuation, f_θ is expected to be proportional to $P_{\rm laser}$. Although Fig. 6 does not clearly show a linear relationship between f_θ and $P_{\rm laser}$ owing to the strong thermal fluctuation, it does show that f_θ increases with $P_{\rm laser}$. One may think a larger $P_{\rm laser}$ would lead to the data with a higher signal-to-noise-ratio. However, the use of larger $P_{\rm laser}$ than those presented in this paper may break the microfluidic channel, possibly because of the temperature increase of the PDMS block, and thus, is avoided.

We estimate the trapping stiffness K as follows. If we use a typical parameter set in the experiment such as m = 1, d_p = 0.2 μm, $P_{\rm laser}$ = 313 mW, and $r_{\rm trap}$ = 1.07 μm, the trapping stiffness K is obtained both experimentally and theoretically as $O(10^{-7})$ N m^{-1} with a single significant digit. Here, K in the experiment is obtained using the law of energy equipartition: $K\sigma_r^2/2 = k_BT/2$, where σ_r^2 is the variance of the radial position distribution around equilibrium. However, theory yields about triple this value of K, maybe owing to the thermal fluctuation. The thermal fluctuation gives the particles the chance to escape the trap, which softens the effect of the trapping potential. The experimental and theoretical values of the trapping stiffness estimated using the above simple approximation agree well. To validate the treatment of $r_p \approx r_{\rm trap}$, $r_p = r_{\rm trap} + \Delta r_{\rm trap}$ is considered in a mechanically strict manner, where $\Delta r_{\rm trap}$ is a displacement that should satisfy the equation $|f^{\rm grad}(|\boldsymbol{r}_n| = r_{\rm trap} + \Delta r_{\rm trap})| = f^{\rm cent}(= m_p r_p \omega^2)$ and the force is the origin of realizing the orbital motion. Using experimentally obtained values of $f^{\rm cent}$ = 5.12 × 10^{-23} N, $\Delta r_{\rm trap}$ must be $O(10^{-16})$ m for the present order of K. Therefore, $\Delta r_{\rm trap}$ can be negligible and is not detectable in the present measuring system mainly due to the spatial resolution of image acquisition and thermal fluctuation. Although the theory may have limitations due to the complexity of phenomena, the detailed mechanics can be clarified. It is also confirmed that the trapping effect represented by K certainly governs the stable orbital motion of nanoparticles.

Furthermore, to quantify the effect of thermal fluctuation, we use the experimental displacement distribution to estimate the diffusion coefficient in the radial and circumferential directions for 50 fps and 1000 fps with $P_{\rm laser}$ = 313 mW. If we assume Wiener diffusion, the displacement forms a Gaussian distribution, and therefore the diffusion coefficient is evaluated by dividing the ensemble average of the mean square displacement by the sampling interval. The mean square displacement is equivalent to the variance of the displacement distribution. We obtain a radial diffusion coefficient of D_r = 1.05 × 10^{-12} m^2 s^{-1} for 50 fps and D_r = 3.51 × 10^{-12} m^2 s^{-1} for 1000 fps. One may think that the diffusion coefficient in the radial direction is affected by the presence of the optical force. This point will be discussed later in this paragraph. Using the same procedure, we obtain a circumferential diffusion coefficient of D_θ = 1.90 × 10^{-12} m^2 s^{-1} for 50 fps and D_θ = 4.00 × 10^{-12} m^2 s^{-1} for 1000 fps. The reason why the diffusion coefficients are underestimated for 50 fps is as follows. On the basis of the overdamped Langevin equation,[53] the characteristic time of a phenomenon is $\tau_0 = \xi/K \approx 10$ ms, where K = 2.42 × 10^{-7} N m^{-1} is the trapping stiffness theoretically obtained as described above. Note that τ_0 is the time in which a nanoparticle is accelerated by the optical force. In other words, the particle

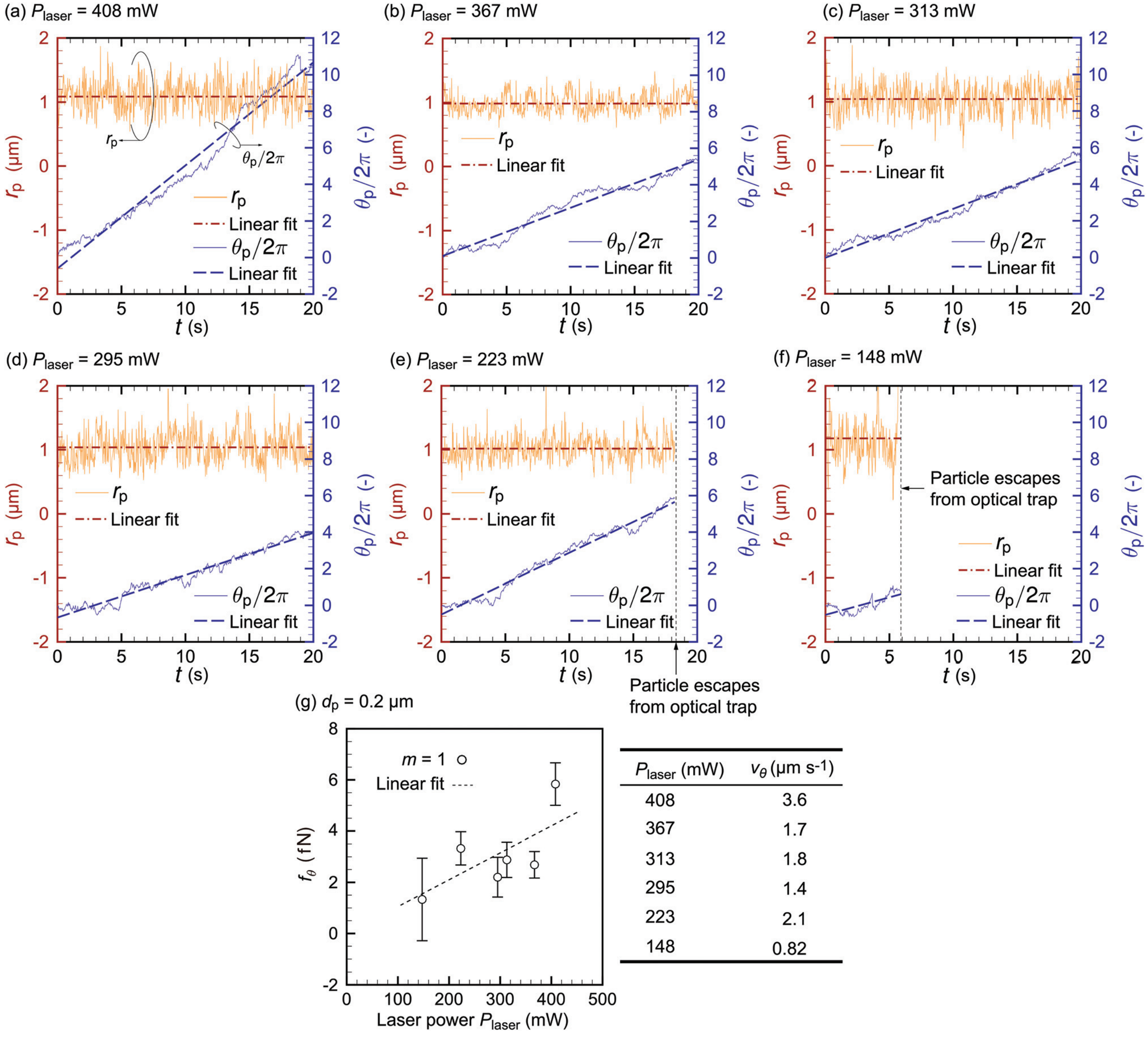

P_{laser} (mW)	v_θ (μm s-1)
408	3.6
367	1.7
313	1.8
295	1.4
223	2.1
148	0.82

Fig. 6 Time development of the orbital radius r_p and circumferential coordinate θ_p for a nanoparticle with diameter d_p = 0.2 μm with laser powers of (a) 408, (b) 367, (c) 313, (d) 295, (e) 223, and (f) 148 mW, where the azimuthal mode is set to be m = 1. (g) Circumferential force f_θ obtained using eqn (3) and the data of panels (a)–(f) for those laser powers. The value of v_θ is also given in panel (g) as a reference.

reflected by an optical potential barrier does not collide with the other barrier at least during τ_0 in the case of overdamping. The time resolution for 1000 fps is 1 ms ($<\tau_0$), and thus the nanoparticle may diffuse freely during the time interval of 1 ms if the optical force is much weaker than the random force. Therefore, it is reasonable to estimate the diffusion coefficient using the overdamped regime in free solutions for the case of 1000 fps. This is the reason why we can evaluate D_r even under the confining optical force in the radial direction. However, the time resolution for 50 fps is 20 ms ($>\tau_0$), and the diffusion coefficient is possibly affected by the optical force. Thus, we suspect that the high frame rate of 1000 fps is better for obtaining a correct diffusion coefficient upon further consideration based on molecular fluid dynamics.[54] In fact, it was reported that the diffusion coefficient obtained from the displacement distribution under an external force was underestimated for data acquired with a large frame interval,[55] where the external force acting on a particle was caused by the confining particle–wall interaction of two parallel walls. The values of D_r and D_θ for 1000 fps slightly overestimate the diffusion coefficient obtained *via* the Stokes–Einstein relationship $D = k_BT/(6\pi a_p\eta) = 2.59 \times 10^{-12}$ m^2 s^{-1}, which may be because the other particles in the orbit enhance the self-diffusion.[56] However, the results show that the particle diffusivity in these experimental conditions is similar to that in bulk solutions. We conclude that the diffusion coefficient may be roughly estimated from the displacement distribution even when the Brownian particle is under an optical external force and has motion characteristics different from those of ordinary diffusion.

(ii) Case of $d_p \geq 0.5$ μm

For $d_p \geq 0.5$ μm, f_θ clearly correlates with P_{laser} linearly because the orbital motion under the optical force is stronger than the thermal fluctuation. Fig. 7 shows the results for the larger diameters 0.5, 1.0, and 2.0 μm for the azimuthal modes (a) $m = 1$, (b) $m = 3$, (c) $m = 5$, and (d) $m = 7$. The number of particles in the orbit, N, is also indicated in the figure for $d_p = 1.0$ and 2.0 μm. We have chosen N so that the line density ρ_L along the orbit has similar values for different modes: that is, $\rho_L \equiv 2\pi r_{trap}/d_p \approx 0.64 \pm 0.03$. In these figures, the circumferential force f_θ obtained using eqn (3) is plotted for various laser powers. First, we find that f_θ linearly correlates with P_{laser} for all m, as expected from eqn (4b) and (6). As d_p increases, f_θ also increases owing to the larger scattering cross section. In contrast, the figure does not show a clear dependence of f_θ on the mode m. Therefore, we rearrange the data in Fig. 7 for each d_p in Fig. 8, which shows f_θ for (a) $d_p = 0.5$, (b) 1.0, and (c) 2.0 μm for various azimuthal modes. Fig. 8 shows no clear qualitative m-dependence, and thus the linear-fit lines are drawn using the data for all the m cases. More specifically, in the case of $d_p = 0.5$ μm (panel (a)), f_θ tends to be larger for $m = 1$ but f_θ takes similar values for $m = 3$, 5, and 7; in the case of $d_p = 1.0$ μm (panel (b)), f_θ tends to be smaller for $m = 1$ but f_θ takes similar values for $m = 3$, 5, and 7; in the case of $d_p = 2.0$ μm (panel (c)), f_θ takes similar values for $m = 1$, 3, 5, and 7. The absence of clear m-dependence is due to the fact that $|f^{scat}|$ is almost independent of m in eqn (8). However, one may think that the experiment shown in Fig. 8 is not well controlled, because $m = 1$ has the highest f_θ value for $d_p = 0.5$ μm (panel (a)) and the lowest value for $d_p = 1.0$ μm (panel(b)). This quantitative inconsistency may be due to the fact that f_θ is a function of N. For $d_p = 1.0$ μm, we will show more quantitatively that the lower f_θ for $m = 1$ than for $m = 3$, 5, and 7 in Fig. 8(b) is due to the N-dependence of f_θ by comparing the experimental results with simulation.

Azimuthal-mode dependence on orbital radius

In this section, the effect of m on the orbital radius r_{trap} is investigated and compared with the simple model of eqn (7).

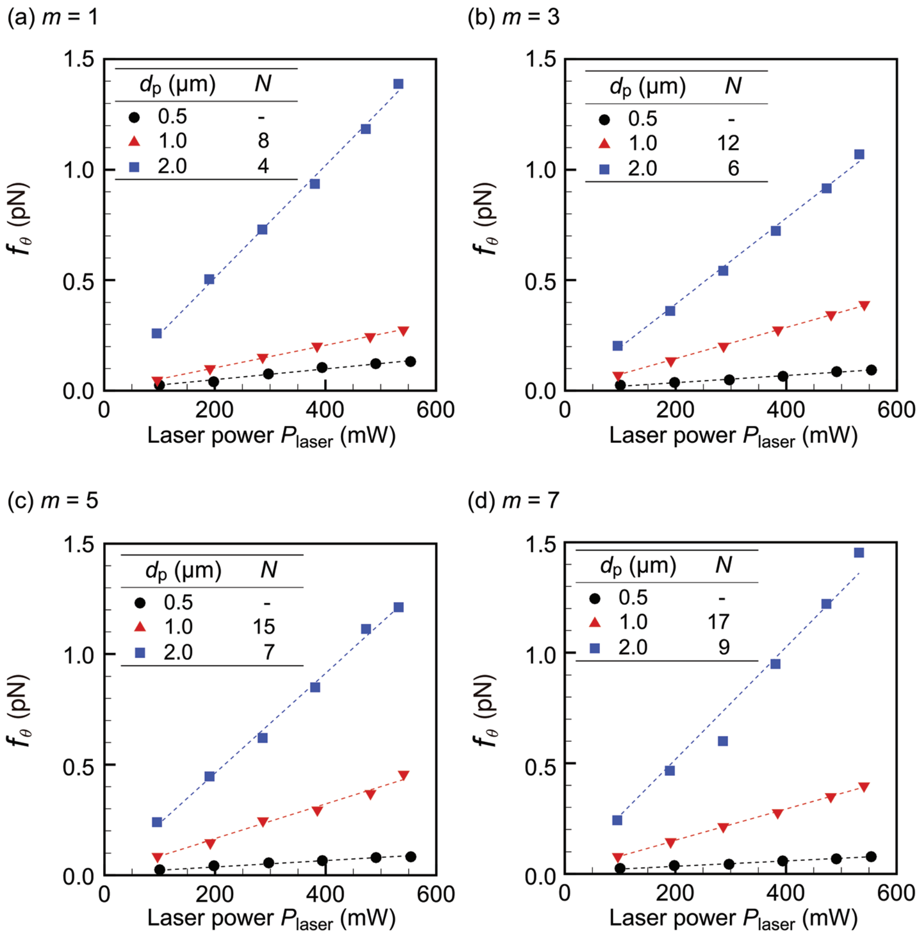

Fig. 7 Laser power dependence of the circumferential force component f_θ for azimuthal modes (a) $m = 1$, (b) $m = 3$, (c) $m = 5$, and (d) $m = 7$. The cases of $d_p = 0.5$, 1.0, and 2.0 μm are shown. The number of particles N trapped in the orbit is also presented for $d_p = 1.0$ and 2.0 μm.

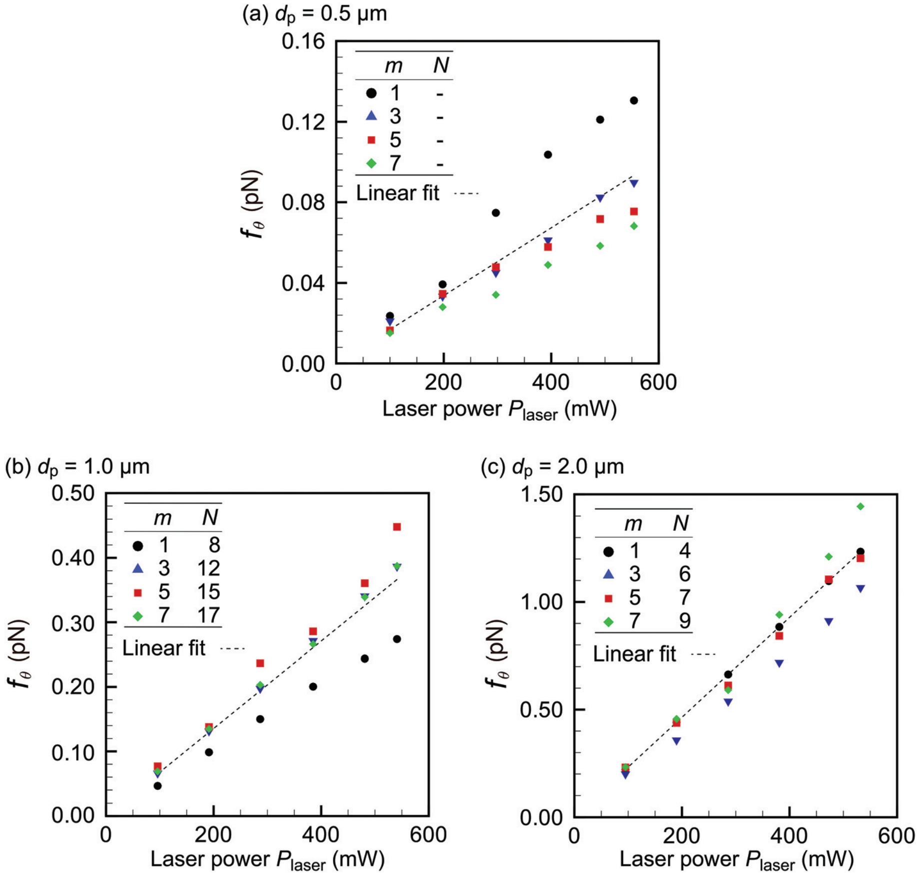

Fig. 8 Laser power dependence of the circumferential force component f_θ for particle diameters (a) 0.5, (b) 1.0, and (c) 2.0 μm. The cases of m = 1, 3, 5, and 7 are shown. The measured number of particles N trapped in the orbit is also presented for d_p = 1.0 and 2.0 μm.

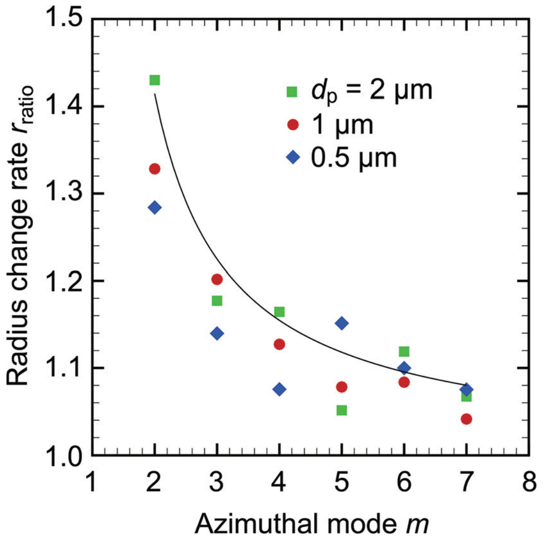

Fig. 9 Relationship between the radius change rate r_{ratio} in eqn (7) and the azimuthal mode m for d_p = 0.5, 1.0, and 2.0 μm. The solid curve represents eqn (7), which is obtained with the Rayleigh approximation.

This is important because predicting r_{trap} contributes to the optimal design of microfluidic channels to use orbital particle motion. Fig. 9 shows the relationship between the radius change rate r_{ratio} defined in eqn (7) and the azimuthal mode m for d_p = 0.5, 1.0, and 2.0 μm. Eqn (7) well approximates the experimental results quantitatively. Although the particles with $d_p \geq 0.5$ μm cannot be considered as a part of the Rayleigh regime, the Rayleigh estimation well predicts the orbital radius r_{trap}. A previous study[52] also found that Rayleigh theory made good predictions of gradient force on particles out of its applicable diameter range. Therefore, we conclude that our method of predicting r_{trap} is a useful first approximation of the orbital radius for engineering applications.

Dependence of the orbital speed on the number of particles

In this section, we investigate the dependence of the orbital motion on the number of particles N, focusing on the cases of d_p = 0.2 and 1.0 μm. As discussed for Fig. 7 and 8, we speculate that there is a correlation between N and orbital speed throughout the experiments. Fig. 10 shows the circumferential force component f_θ and the corresponding angular frequency $\omega \equiv v_\theta / r_{trap}$ for d_p = 1.0 μm with (a) m = 1 and (b) m = 2 as functions of N. For smaller N values not shown in the figure, multiple particles do not move smoothly in orbits but do have

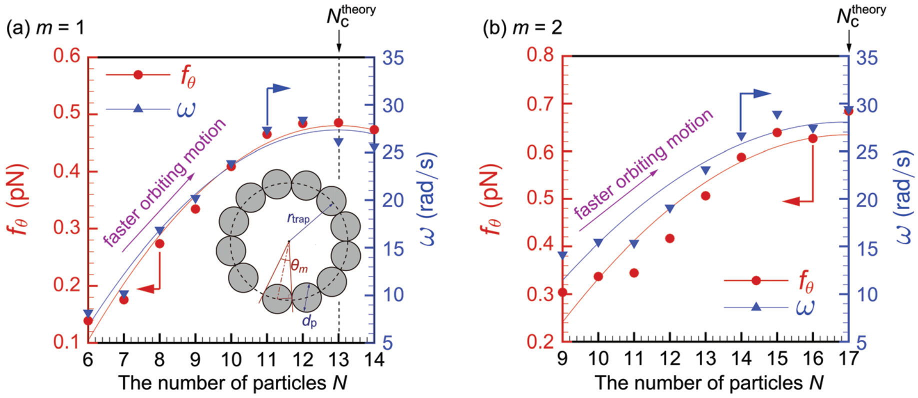

Fig. 10 Experimental results for f_θ and ω as functions of the number of particles N for (a) m = 1 and (b) m = 2 with d_p = 1.0 µm. The angle occupied by a single particle, θ_m, is calculated using r_{trap} obtained in the experiment: r_{trap} = 2.10 µm for m = 1 and 2.73 µm for m = 2. Note that the increase of N leads to faster orbiting motion with higher ω.

rhythmic motion, as reported elsewhere,[11] or are trapped at a certain θ_p. A part of raw data is presented in Fig. 13 in Appendix C. Both f_θ and ω increase as N increases, meaning the orbital speed increases, up to a critical value N_c = 12 for (a) and 15 for (b); f_θ and ω are less affected by N for $N \geq N_c$. To investigate the relationship between f_θ and particle occupancy in the orbit, we compute N_c^{theory} from geometrical considerations. The inset of Fig. 10(a) is the schematic of particles with diameter d_p contained in an orbit of radius r_{trap}, where θ_m is an angle occupied by a single particle. We obtain N_c^{theory} as the integer part of $2\pi/\theta_m$, which leads to N_c^{theory}= 13 and 17 for m = 1 and 2, respectively. These values are close to those observed in the experiments. We conclude that the angular frequency ω of orbiting particles increases with N and approaches a constant value as N approaches N_c owing to the geometrical restriction. In this paper, we avoid discussing the cases with a larger number of particles than presented, since the particle configuration becomes complicated for $N \geq N_c$, *e.g.*, additional particles may squeeze and deform the filled orbit, or may stick to the outer side of the orbit. Therefore, it is difficult to classify these configurations and investigate them systematically. Further investigation of the configuration of multiple necklace that will appear in the case with $N \gg N_c$ is left for future study.

We carry out a numerical simulation based on our model in eqn (1b)–(6) to reveal the origin of the N-dependence of angular frequency observed in the experiments. The parameters in the simulation are similar to those in the experiments: P_{laser} is set to be 500 mW, and w_0 is obtained from the relationship $r_{trap} = w_0\sqrt{m/2}$ with r_{trap} = 2.1 µm, which is obtained experimentally with m = 1 and the OL with a magnification of 20×. In preliminary computations, we find that eqn (4b) overestimates the experimental values of ω by a factor of approximately 10. This overestimation by the simulation may be due to the overestimation of the scattering force and/or the increase of viscosity η in the experiment, which arises because of the wall effect and/or the addition of surfactant. Therefore, we multiply the scattering force by S_c = 0.1 to obtain values of ω that are comparable to the experimental values in Fig. 10. This inconsistency will be closely investigated in future work by including the effects of the wall and surfactant in the model. One may think that S_c should also multiply the gradient force in eqn (4c). However, doing so results in the situation where some particles cannot be kept in the orbit when two or more of them are close to each other. This behavior is not observed in our experiments, and thus multiplying the gradient force by S_c is even qualitatively inconsistent with observation. Therefore, we only multiply the scattering force by S_c. The value S_c = 0.1 is used throughout the paper because it yields moderate agreement between theory and experiment for different particle diameters and azimuthal modes.

Let us describe the result for d_p = 1 µm. Fig. 11(a) shows the simulation results for ω, where m = 1, 2, 3, 5, and 7. First, we focus on the profiles for m = 1 and 2, which correspond to the experimental results in Fig. 10(a) and (b), respectively. Fig. 11(b) shows the comparison between the simulation and the experiment. Because we introduced the fitting parameter S_c = 0.1, the experimental values of ω agree well with the simulated values of ≈10–30 rad s^{-1}. The remarkable agreement to be noted is that both the simulation and the experiment show the increase of ω for increasing N up to a critical value $N \leq N_c$. Moreover, ω shows a different trend for $N > N_c$ in both the simulation and the experiment: the rate of increase becomes low. Therefore, the N-dependency observed in the experiment in Fig. 10 is well explained qualitatively by our simulation model. However, for more a quantitative comparison, we remark that the effects of the imperfection of the LG beam or of the presence of particles on the electromagnetic field should be carefully taken into account. Because these are extremely difficult problems and complicate the discussion, we leave them for the constitutive investigation in future research and focus mainly on the effect of N in this paper. Given a qualitative agreement between the simulation and experiments, we conclude that the hydrodynamic inter-particle interaction, which becomes strong as N increases, significantly affects the orbital speed. Fig. 11(a) shows that the effect of this hydrodynamic interaction is weaker for higher m. We attribute

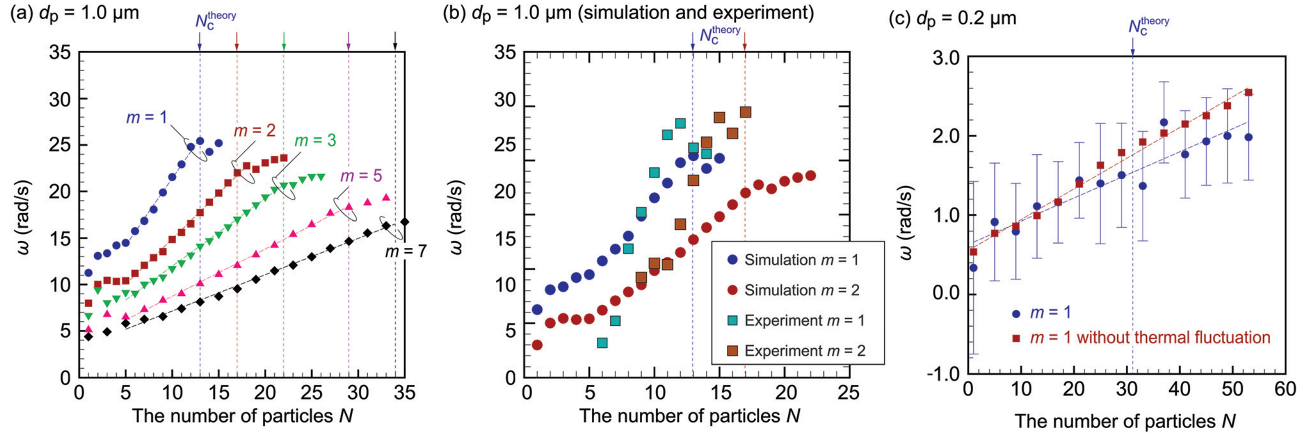

Fig. 11 (a) Simulation results for ω as a function of the number of particles N for m = 1, 2, 3, 5, and 7 with d_p = 1.0 μm and P_{laser} = 500 mW. The orbital frequency ω increases as N increases owing to the hydrodynamic inter-particle interaction. (b) Comparison between the simulation results for m = 1 and 2 in panel (a) and the experimental results in Fig. 10. (c) Simulation results for ω for m = 1 with d_p = 0.2 μm, including the results without thermal fluctuation.

this to the increase of $r_{\text{trap}} \sim \sqrt{m}$ for higher m. More precisely, the distance $|\boldsymbol{r}_{nn'}|$ between particles in eqn (2) increases when r_{trap} increases, leading to lower $|\boldsymbol{f}_n^{\text{hydr}}|$.

Next, we compare the resulting f_θ values for m = 1, 3, 5, and 7 between the simulation in Fig. 11(a) and the experiment in Fig. 8(b). The goal of this comparison is to understand the m-dependence of f_θ in Fig. 8(b). The results are summarized in Table 2, where f_θ is normalized by dividing its values for m = 3, 5, and 7 by that for m = 1. The qualitative behavior is consistent between theory and experiment. Therefore, the subtle m-dependence of f_θ in Fig. 8(b) is due to the different values of N.

Finally, Fig. 11(c) presents the simulation result for d_p = 0.2 μm. In the experiment, the orbital motion of these particles is the least stable owing to the weak optical force. Recall that the scattering cross sections are $\sigma^2 = 8.53 \times 10^{-1}$ μm^2 for d_p = 1 μm and $\sigma^2 = 4.31 \times 10^{-4}$ μm^2 for d_p = 0.2 μm. The weakness of the scattering force may be why there are no previous studies on dielectric particles with a diameter of 0.2 μm or less. In our experiments, we clearly observe the orbital motion of dielectric particles with d_p = 0.2 μm using a microfluidic channel with no biased background fluid flow and a mixture of fluorescent and non-fluorescent particles, as shown in Fig. 4 (a1)–(a3) and 6. The corresponding simulation is carried out to show that the hydrodynamic effect on ω is also significant for d_p = 0.2 μm. The beam waist w_0 is obtained from the relationship $r_{\text{trap}} = w_0\sqrt{1/2}$ with an experimental value of r_{trap} = 1.0 μm. Fig. 11(c) shows the relationship between ω and N. The effect of thermal fluctuation is significant for d_p = 0.2 μm, and thus ω has larger stochastic fluctuation. Ensemble averages over 10 runs are taken to reduce stochastic noise, and the error bars in Fig. 11(c) show the standard deviation. The results without thermal fluctuation are also plotted for reference in Fig. 11(c), and a little quantitative difference between the plots with and without thermal fluctuation is observed. We find that single-particle orbital motion, N = 1, is difficult to observe because ω is overwhelmed by the thermal fluctuation. As N increases, ω also increases and eventually overcomes the fluctuation, leading to $\omega \approx 1.5$ rad s^{-1} at $N = N_c^{\text{theory}}$, which means about 0.25 Hz. The experimental value of ω is ω = 3.31 rad s^{-1}, which is on the same order as the simulation value. Therefore, we conclude that the hydrodynamic interaction between particles increases the orbital speed even for d_p = 0.2 μm. This is the key to inducing the orbital motion of small dielectric particles.

Table 2 Comparison between the experiment (Fig. 8(b)) and simulation (Fig. 11(a)). The force is normalized by dividing the values of f_θ for m = 3, 5, and 7 by that for m = 1

	m = 1 N = 8	m = 3 N = 12	m = 5 N = 15	m = 7 N = 17
Experiment (Fig. 8(b))				
ω (rad s^{-1})	16.9	14.9	14.2	10.9
f_θ (fN)	275	385	450	385
Normalized f_θ (—)	1.00	1.40	1.63	1.40
Simulation (Fig. 11(a))				
ω (rad s^{-1})	18.0	13.2	11.1	9.53
f_θ (fN)	291	367	399	406
Normalized f_θ (—)	1.00	1.26	1.37	1.39

Contribution of each force component

In this section, we estimate the contributions of forces acting on a single nanoparticle, the nth particle in the orbit. Particularly, we estimate the contributions of the circumferential forces $f_n^{\text{scat}} = |\boldsymbol{f}^{\text{scat}}(\boldsymbol{r}_n)|$ and $f_n^{\text{hydr}} = |\boldsymbol{f}_n^{\text{hydr}} \cdot \boldsymbol{e}_{n,\theta}|$ and the radial force $f_n^{\text{grad}} = |\boldsymbol{f}^{\text{grad}}(\boldsymbol{r}_n)|$ in eqn (1b) and (4), using P_{laser} = 313 mW and d_p = 0.2 μm. First, let us consider the radial direction. We take $r = r_{\text{trap}} + \Delta r$ as the reference position to evaluate the radial component of the optical force f_n^{grad}, where Δr = 0.22 μm is the standard deviation from $r = r_{\text{trap}}$ in the experiment. Then, we obtain f_n^{grad} = 53.1 fN, which we consider the reference radial component of the optical force. We also compute the potential energy at the reference displacement as $(1/2)K(\Delta r)^2 = 5.86 \times 10^{-21}$ J, which is comparable to but slightly greater than the thermal fluctuation $(1/2)k_\mathrm{B}T = 2.07 \times 10^{-21}$ J. This estimate explains the stable orbital motion for P_laser = 313 mW, as observed in Fig. 6, and the unstable one for the lower laser power of 148 mW in the experiment. However, the circumferential component f_n^scat acting on a single particle is theoretically estimated as 0.56 fN with $S_\mathrm{c} = 0.1$, which is much lower than the radial component. This may be why it is difficult for a single nanoparticle to undergo orbital motion. We then estimate the simulated hydrodynamic force f_n^hydr for $N = N_\mathrm{c}^\text{theory} = 31$ and obtain 1.41 fN. The hydrodynamic force is 2.5 times stronger than the scattering force acting on a single particle, and thus the hydrodynamic interaction is dominant in the circumferential direction. The magnitude of repulsive force is about 0.01 fN and negligible. The theoretically estimated circumferential force is thus $f_\theta = f_n^\text{scat} + f_n^\text{hydr} = 1.97$ fN, which underestimates the experimentally obtained $f_\theta = 2.92$ fN in Fig. 6(g). We speculate that N in the experiment is larger than $N_\mathrm{c} = 31$, leading to a stronger circumferential force in the experiment than in the theory.

The significance of the hydrodynamic effect is explained theoretically as follows. Considering N particles as a single aggregate, as shown in Fig. 12(a) for $N = 4$, the net circumferential component of optical forces acting on the aggregate is proportional to N. However, the net drag force acting on the aggregate can be analytically obtained as $C_N f^\text{drag}$ if we approximate the aggregate as a line moving with speed v, as shown in Fig. 12(b).[57] We use $f^\text{drag} = 6\pi\eta av$ as the Stokes drag. The analytical form of C_N depends on N and the distance ℓ between particles, and is given in the literature for N up to 4.[57] More specifically, C_N is in the range $1 \leq C_N \leq N$, as shown in Fig. 12(b); that is, the net drag force $C_N f^\text{drag}$ is less than the superposition of the drag forces acting on N single particles, Nf^drag. Therefore, assuming the linear aggregate in Fig. 12(b), we obtain the analytical form of v_θ as $v_\theta^\text{(anal)} = Nf_n^\text{scat}(C_N 6\pi\eta a)^{-1}$. The values of $v_\theta^\text{(anal)}$ for $\ell = 2a$ are presented in Fig. 12(c). We carry out the simulation without thermal fluctuation to compare the simulation results with these analytical values. We use a harmonic potential to fix the distances between the particles at $\ell \approx 2a$ as in the analytical result. Fig. 12(c) also presents the values of the simulated speed $v_\theta^\text{(sim)}$, under the condition $\ell/2a < 1.05$. We find that $v_\theta^\text{(anal)}$ and $v_\theta^\text{(sim)}$ agree well, as do their rates of increase with respect to N. Therefore, even though the net optical and drag forces acting on the aggregate both increase with N, the rate of increase for the net optical force overtakes that of the net drag force. The above estimate

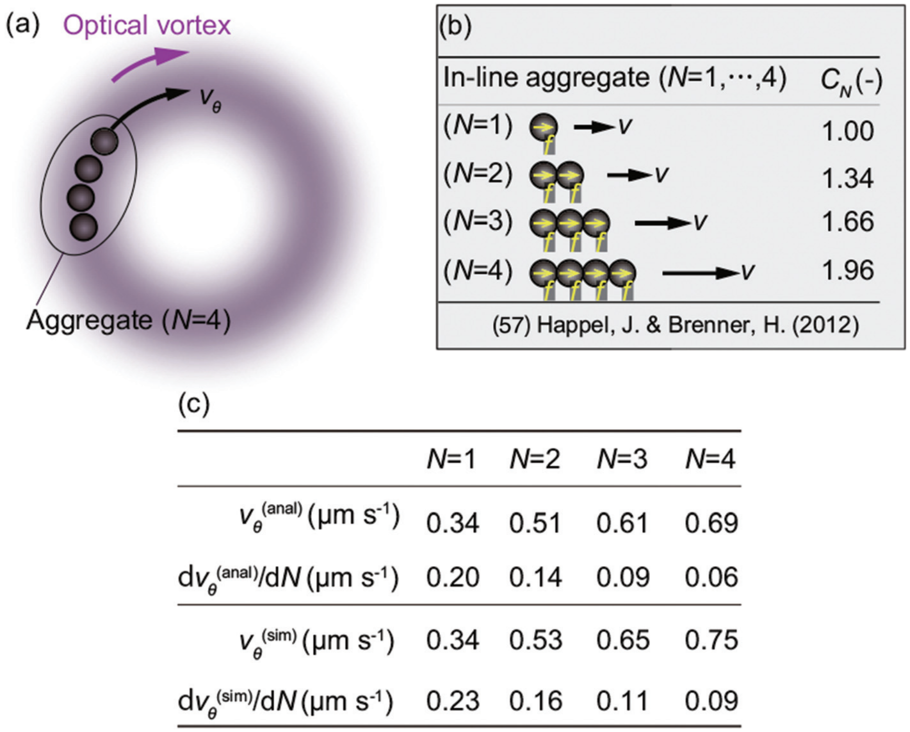

In-line aggregate (N=1,⋯,4)		C_N(-)
(N=1)	→ v	1.00
(N=2)	→ v	1.34
(N=3)	→ v	1.66
(N=4)	→ v	1.96

(57) Happel, J. & Brenner, H. (2012)

	N=1	N=2	N=3	N=4
$v_\theta^{(\text{anal})}$ (μm s^{-1})	0.34	0.51	0.61	0.69
d$v_\theta^{(\text{anal})}$/dN (μm s^{-1})	0.20	0.14	0.09	0.06
$v_\theta^{(\text{sim})}$ (μm s^{-1})	0.34	0.53	0.65	0.75
d$v_\theta^{(\text{sim})}$/dN (μm s^{-1})	0.23	0.16	0.11	0.09

Fig. 12 Comparison between simulation and analytical results. (a) An N-particle system under the optical vortex is approximated as a single aggregate. The cases up to N = 4 are illustrated. (b) Schematic of a linear aggregate.[57] Because d_p = 0.2 μm is smaller than the orbital radius r_trap = 1.07 μm, we assume that the aggregate in (a) is approximately linear, as shown in (b). The drag force acting on the linear aggregate is a modified Stokes drag $C_N(6\pi\eta av)$, where C_N is a numeric constant depending on N whose analytical form is given in ref. 57. The analytical form of the velocity v of the linear aggregate is obtained as $v = Nf(6\pi\eta aC_N)$, where f is an external force acting on each particle. (c) Analytical result $v_\theta^{(\text{anal})}$ approximated by $v = Nf/(6\pi\eta aC_N)$ in panel (b) and the simulation result $v_\theta^{(\text{sim})}$ of panel (a) for N = 1,…4, d_p = 0.2 μm, P_laser = 313 mW, and m = 1. The rate of increase, dv_θ/dN, obtained with the second-order finite-difference scheme is also given.

shows that the hydrodynamic inter-particle interaction is significant in the orbital motion of nanoparticles.

Concluding remarks

This study has used both experiment and theory to show that hydrodynamic inter-particle interaction increases the orbital speed of nano- and microparticles with diameters from 0.2 to 2.0 μm irradiated by an optical vortex consisting of a focused LG beam with a wavelength of 1064 nm. The experiments achieved stable optical trapping of dielectric nanoparticles even with inherent thermal fluctuation, using the assistance of hydrodynamic inter-particle interaction and microchannel confinement in the direction of laser irradiation. The confinement helps stable trapping by restricting the motion of Brownian particles to two dimensions. Using the radial component of the orbital motion of a trapped particle, we evaluated the optical forces by comparing them with the thermal fluctuation. For the circumferential component, we found both experimentally and theoretically that the orbital speed increased with the number of trapped particles. The diameter of the orbit increased as the azimuthal mode of the optical vortex increased, but the orbital speed was seemed not to be affected by the azimuthal mode when the number density of the particles in the orbit was same. We achieved single-particle tracking in the presence of many other nanoparticles using a mixture of fluorescent and non-fluorescent particles. A theoretical model was developed that included hydrodynamic inter-particle interaction to analyze the experimentally observed behavior of the number of trapped particles, and a micro- and nanofluid dynamics simulation was carried out. The optical force was evaluated from the trapping stiffness in the radial direction. Reasonable agreement was found between the theory and experiment, validating the proposed model. Simulating the model showed qualitatively that the hydrodynamic inter-particle interaction enhances the orbiting speed of micro- and nanoparticles, and the simulation results well explained the number-of-particles dependence and the azimuthal-mode dependence observed in the experiments. These techniques will contribute to the optical manipulation of dielectric micro- and nanoparticles with small polarizability, such as cells and viruses in biosciences. Our future work will apply this technique for controlling nanoparticles in micro- and nanofluidic devices.

Conflicts of interest

There are no conflicts to declare.

Appendix A: fabrication of the silicon mold

An silicon-on-insulator (SOI) wafer (AD004, Sumco Corp., Tokyo, Japan) is used to fabricate the mold for microfluidic devices. The wafer has an SOI layer with a thickness of 3 ± 0.75 μm on the silicon substrate. First, a resist mask is fabricated on the SOI layer using standard photolithography. Then, we carry out deep reactive-ion-etching (RIE) of the SOI layer to fabricate a channel pattern on the silicon substrate. The RIE depth is determined by the thickness of the SOI layer.

The microchannel has contraction parts with a length scale of 3 μm. These contraction parts are prepared to increase the hydraulic resistance R_h over the channel and to increase the flow control resolution. Note that the unexpected flow speed u in the x-direction in the channel is proportional to $\Delta P/R_\mathrm{h}$, where ΔP is the pressure difference. Therefore, higher R_h is preferred to achieve lower u. In our experiments, u should be as low as possible to eliminate the effect of the mean flow on the orbiting motion of particles.

The mold has a micrometer-scale pattern with an aspect ratio approximately equal to unity. It is difficult to demold a cured PDMS block with such a fine mold structure because the PDMS sticks to the fine mold pattern and breaks during demolding. To avoid the sticking of the PDMS to the fine pattern, the mold is covered with a self-assembled monolayer (SAM) of 1*H*,1*H*,2*H*,2*H*-perfluorodecyltriethoxysilane. The process of SAM coating is as follows. First, the mold is carefully cleaned using ultra-sonication in acetone and 2-propanol for 3 minutes. Then, the mold is baked at 120 °C to remove the residual organic solvents. The mold is exposed to ultraviolet light (PL16, Sen Light Corp., Osaka, Japan) for 10 minutes for further cleaning. The cleaned mold is put in a perfluoroalkoxy alkane (PFA) container. In this container we also put a smaller PFA container including a few drops of 1*H*,1*H*,2*H*,2*H*-perfluorodecyltriethoxysilane solution. After tightly closing the larger PFA container, we put it in an oven (Do-300, RB Technology, Fukuoka, Japan) and heat it at 120 °C for 3 hours. The evaporated solution forms the SAM layer on the mold. The presence of the SAM layer, which is highly hydrophobic, is verified using the droplet method. The contact angle of a water droplet on the mold is improved from 66° before treatment to 106° after treatment, and the formation of the SAM layer is confirmed. Now, we can safely demold the PDMS without breaking the fine pattern.

Appendix B: confirmation of Stokes drag on an orbiting particle

Let us suppose that the center of a sphere is orbiting with a circumferential speed $v_\theta = r_\mathrm{trap}\omega$, where ω is the angular frequency. The outer part of the sphere, $r = r_\mathrm{trap} + d_\mathrm{p}/2$, experiences relative flow $v_\theta{}^\mathrm{rel} = (r_\mathrm{trap} + d_\mathrm{p}/2)\omega - v_\theta = (d_\mathrm{p}/2)\omega$. Therefore, we can approximate the drag acting on the orbiting sphere as that on a sphere placed in a shear flow with a non-dimensional shear rate $\kappa = v_\theta^\mathrm{rel}/v_\theta$. The experimental results show that the shear rate is $\kappa = (d_\mathrm{p}/2)/r_\mathrm{trap} = O(1)$. The correction to the Stokes drag, including lift force, due to the shear rate κ is $O\left(\sqrt{\kappa \mathrm{Re}}\right)$,[58] where Re in this study is $O(10^{-7})$. Therefore, the correction to the Stokes drag is 0.1% at most, and we can safely use Stokes flow dynamics for this study.

Appendix C: θ_p dependence of the angular frequency

The θ_p-dependence of the orbital angular frequency ω for the data of Movie S1† and Fig. 10(a) are given in Fig. 13. In Fig. 13, the number of particles in the orbit is set to be (a) $N = 6$, (b) 8, (c) 10, and (d) 12. The laser power $P_{\text{laser}} = 541$ mW and the azimuthal mode $m = 1$ are used. Locally averaged data (large red symbol) are obtained by averaging the raw data of ω (small symbol) in an interval of width $\Delta\theta_p = 2\pi/25$, and the error bars represent the standard deviation. Blue-bold solid lines show the average for all raw data. Standard deviations σ_{dev} of the locally averaged data from the mean value are evaluated as (a) $\sigma_{\text{dev}} = 11.2$, (b) 15.2, (c) 9.75, and (d) 8.27 rad s^{-1}. It is seen that ω depends on θ_p and takes large values around $\theta_p/2\pi \approx 0.2$ for all N, which may be attributed to the imperfection of the ring. The averaged quantities (blue-bold solid lines), which are used in the main text, show the clear increase as the number of particles N.

The θ_p-dependence may be caused by the characteristics of our optical system, but also may be due to the effects of the presence of charged particles and induced solvent flow on the electromagnetic field. These are extremely difficult problems and beyond the scope of the present paper, we leave them for constitutive investigation in future research. Nonetheless, we carry out a similar experiment using a different objective lens with a higher NA value (NA = 1.4, 40× magnification, oil immersion, UPLXAPO40XO, Olympus) to see whether the θ_p-dependence can be reduced in a different optical setup. The result is given in Fig. 14, where the panel (a) shows the snap-

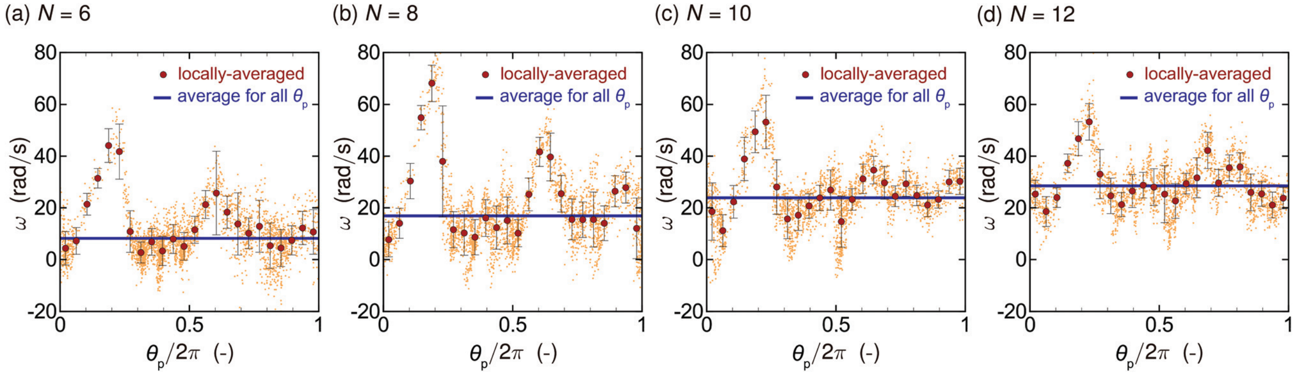

Fig. 13 θ_p-Dependence of the orbital angular frequency ω for the particle with the diameter $d_p = 1$ μm and for the number of particles in the orbit (a) $N = 6$, (b) 8, (c) 10, and (d) 12. The laser power $P_{\text{laser}} = 541$ mW and the azimuthal mode $m = 1$ are used. Locally averaged data (large red symbol) are obtained by averaging the raw data of ω (small symbol) in an interval of width $\Delta\theta_p = 2\pi/25$, and the error bars represent the standard deviation. Blue-bold solid lines show the average for all raw data. The averaged quantities (blue-bold solid lines), which are used in the main text, show the clear increase as the number of particle N.

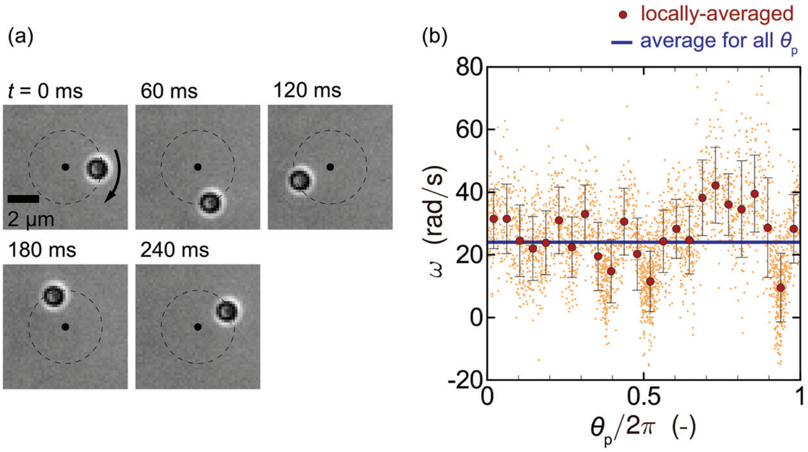

Fig. 14 (a) Orbital motion of a single particle obtained with a different objective lens with higher NA value (NA = 1.4, 40× magnification, oil immersion, UPLXAPO40XO, Olympus) using parameters $P_{\text{laser}} = 93$ mW, $m = 7$, and $d_p = 1$ μm. (b) θ_p-Dependence of the orbital angular frequency ω.

shots of the orbital motion using the parameters P_{laser} = 93 mW, m = 7, and d_{p} = 1 μm with N = 1. It is seen that the single particle orbiting is observed, and Fig. 14(b) presents the θ_{p}-dependence of the orbital angular frequency ω for Fig. 14(a). The standard deviation σ_{dev} of the locally averaged data from the mean value is σ_{dev} = 8.26 rad s^{-1} and is smaller than those in Fig. 13. However, the complete elimination of the θ_{p}-dependence is difficult in the present experimental setup. Therefore, we discuss the averaged quantities (blue-bold solid lines) in the main text.

Acknowledgements

This study was supported by the Japan Society for the Promotion of Science (JSPS) KAKENHI under Grant Number JP18H05242 for Scientific Research (S), Grant Number JP16H06504 for Scientific Research on Innovative Areas (Nano-Material Optical-Manipulation), and Grant Number JP18K13687 for Young Scientists; and the Frontier Photonic Sciences Project of the National Institutes of Natural Sciences under Grant Number 01211901.

References

1 L. Allen, M. Beijersbergen, R. Spreeuw and J. Woerdman, Orbital angular momentum of light and the transformation of Laguerre-Gaussian laser modes, *Phys. Rev. A*, 1992, **45**, 8185.

2 S. Barnett and L. Allen, Orbital angular momentum and nonparaxial light beams, *Opt. Commun.*, 1994, **110**, 670–678.

3 J. Courtial, K. Dholakia, L. Allen and M. Padgett, Gaussian beams with very high orbital angular momentum, *Opt. Commun.*, 1997, **144**, 210–213.

4 J. Curtis and D. Grier, Structure of optical vortices, *Phys. Rev. Lett.*, 2003, **90**, 133901.

5 S. Tao, X. Yuan, J. Lin, X. Peng and H. Niu, Fractional optical vortex beam induced rotation of particles, *Opt. Express*, 2005, **13**, 7726–7731.

6 Y. Roichman, D. G. Grier and G. Zaslavsky, Anomalous collective dynamics in optically driven colloidal rings, *Phys. Rev. E*, 2007, **75**, 020401.

7 Y. Sokolov, D. Frydel, D. G. Grier, H. Diamant and Y. Roichman, Hydrodynamic pair attractions between driven colloidal particles, *Phys. Rev. Lett.*, 2011, **107**, 158302.

8 Y. Sassa, S. Shibata, Y. Iwashita and Y. Kimura, Hydrodynamically induced rhythmic motion of optically driven colloidal particles on a ring, *Phys. Rev. E*, 2012, **85**, 061402.

9 H. Nagar and Y. Roichman, Collective excitations of hydrodynamically coupled driven colloidal particles, *Phys. Rev. E*, 2014, **90**, 042302.

10 S. Okubo, S. Shibata, Y. S. Kawamura, M. Ichikawa and Y. Kimura, Dynamic clustering of driven colloidal particles on a circular path, *Phys. Rev. E*, 2015, **92**, 032303.

11 Y. Kimura, Hydrodynamically induced collective motion of optically driven colloidal particles on a circular path, *J. Phys. Soc. Jpn.*, 2017, **86**, 101003.

12 K. Saito, S. Okubo and Y. Kimura, Change in collective motion of colloidal particles driven by an optical vortex with driving force and spatial confinement, *Soft Matter*, 2018, **14**, 6037–6042.

13 H. He, M. Friese, N. Heckenberg and H. Rubinsztein-Dunlop, Direct observation of transfer of angular momentum to absorptive particles from a laser beam with a phase singularity, *Phys. Rev. Lett.*, 1995, **75**, 826.

14 A. T. O'neil and M. J. Padgett, Three-dimensional optical confinement of micron-sized metal particles and the decoupling of the spin and orbital angular momentum within an optical spanner, *Opt. Commun.*, 2000, **185**, 139–143.

15 A. O'neil, I. MacVicar, L. Allen and M. Padgett, Intrinsic and extrinsic nature of the orbital angular momentum of a light beam, *Phys. Rev. Lett.*, 2002, **88**, 053601.

16 M. Dienerowitz, M. Mazilu, P. J. Reece, T. F. Krauss and K. Dholakia, Optical vortex trap for resonant confinement of metal nanoparticles, *Opt. Express*, 2008, **16**, 4991–4999.

17 P. Figliozzi, N. Sule, Z. Yan, Y. Bao, S. Burov, S. K. Gray, S. A. Rice, S. Vaikuntanathan and N. F. Scherer, Driven optical matter: Dynamics of electrodynamically coupled nanoparticles in an optical ring vortex, *Phys. Rev. E*, 2017, **95**, 022604.

18 K. Gahagan and G. Swartzlander, Optical vortex trapping of particles, *Opt. Lett.*, 1996, **21**, 827–829.

19 V. Garcés-Chávez, K. Volke-Sepulveda, S. Chávez-Cerda, W. Sibbett and K. Dholakia, Transfer of orbital angular momentum to an optically trapped low-index particle, *Phys. Rev. A*, 2002, **66**, 063402.

20 M. Reichert and H. Stark, Circling particles and drafting in optical vortices, *J. Phys.: Condens. Matter*, 2004, **16**, S4085.

21 J. Ng, Z. Lin and C. Chan, Theory of optical trapping by an optical vortex beam, *Phys. Rev. Lett.*, 2010, **104**, 103601.

22 M. Tamura, T. Omatsu, S. Tokonami and T. Iida, Interparticle-interaction-mediated anomalous acceleration of nanoparticles under light-field with coupled orbital and spin angular momentum, *Nano Lett.*, 2019, **19**, 4873–4878.

23 R. Nagura, T. Tsujimura, T. Tsuji, K. Doi and S. Kawano, Coarse-grained particle dynamics along helical orbit by an optical vortex irradiated in photocurable resins, *OSA Continuum*, 2019, **2**, 400–415.

24 J. A. Briggs, K. Grünewald, B. Glass, F. Förster, H.-G. Kräusslich and S. D. Fuller, The mechanism of HIV-1 core assembly: insights from three-dimensional reconstructions of authentic virions, *Structure*, 2006, **14**, 15–20.

25 N. M. Bouvier and P. Palese, The biology of influenza viruses, *Vaccine*, 2008, **26**, D49–D53.

26 K. Toyoda, K. Miyamoto, N. Aoki, R. Morita and T. Omatsu, Using optical vortex to control the chirality of twisted metal nanostructures, *Nano Lett.*, 2012, **12**, 3645–3649.

27 F. Takahashi, K. Miyamoto, H. Hidai, K. Yamane, R. Morita and T. Omatsu, Picosecond optical vortex pulse illumination forms a monocrystalline silicon needle, *Sci. Rep.*, 2016, **6**, 21738.

28 M. Watabe, G. Juman, K. Miyamoto and T. Omatsu, Light induced conch-shaped relief in an azo-polymer film, *Sci. Rep.*, 2014, **4**, 4281.

29 D. Barada, G. Juman, I. Yoshida, K. Miyamoto, S. Kawata, S. Ohno and T. Omatsu, Constructive spin-orbital angular momentum coupling can twist materials to create spiral structures in optical vortex illumination, *Appl. Phys. Lett.*, 2016, **108**, 051108.

30 J. Lee, Y. Arita, S. Toyoshima, K. Miyamoto, P. Panagiotopoulos, E. M. Wright, K. Dholakia and T. Omatsu, Photopolymerization with light fields possessing orbital angular momentum: generation of helical microfibers, *ACS Photonics*, 2018, **5**, 4156–4163.

31 M. Chen, M. Mazilu, Y. Arita, E. M. Wright and K. Dholakia, Dynamics of microparticles trapped in a perfect vortex beam, *Opt. Lett.*, 2013, **38**, 4919–4922.

32 M. Chen, M. Mazilu, Y. Arita, E. M. Wright and K. Dholakia, Creating and probing of a perfect vortex in situ with an optically trapped particle, *Opt. Rev.*, 2015, **22**, 162–165.

33 E. K. Sackmann, A. L. Fulton and D. J. Beebe, The present and future role of microfluidics in biomedical research, *Nature*, 2014, **507**, 181.

34 U. F. Keyser, Controlling molecular transport through nanopores, *J. R. Soc., Interface*, 2011, **8**, 1369–1378.

35 D. G. Grier, A revolution in optical manipulation, *Nature*, 2003, **424**, 810.

36 K. C. Neuman and S. M. Block, Optical trapping, *Rev. Sci. Instrum.*, 2004, **75**, 2787–2809.

37 T. Sugiyama, K.-i. Yuyama and H. Masuhara, Laser trapping chemistry: from polymer assembly to amino acid crystallization, *Acc. Chem. Res.*, 2012, **45**, 1946–1954.

38 O. M. Maragò, P. H. Jones, P. G. Gucciardi, G. Volpe and A. C. Ferrari, Optical trapping and manipulation of nanostructures, *Nat. Nanotechnol.*, 2013, **8**, 807.

39 A. Lehmuskero, P. Johansson, H. Rubinsztein-Dunlop, L. Tong and M. Kall, Laser trap ping of colloidal metal nanoparticles, *ACS Nano*, 2015, **9**, 3453–3469.

40 F. Nito, T. Shiozaki, R. Nagura, T. Tsuji, K. Doi, C. Hosokawa and S. Kawano, Quantitative evaluation of optical forces by single particle tracking in slit-like microfluidic channels, *J. Phys. Chem. C*, 2018, **122**, 17963–17975.

41 T. Tsuji, Y. Matsumoto and S. Kawano, Flow with nanoparticle clustering controlled by optical forces in quartz glass nanoslits, *Microfluid. Nanofluid.*, 2019, **23**, 126.

42 A. Ashkin, J. M. Dziedzic, J. Bjorkholm and S. Chu, Observation of a single-beam gradient force optical trap for dielectric particles, *Opt. Lett.*, 1986, **11**, 288–290.

43 S. Tanaka, M. Tsutsui, H. Theodore, H. Yuhui, A. Arima, T. Tsuji, K. Doi, S. Kawano, M. Taniguchi and T. Kawai, Tailoring particle translocation via dielectrophoresis in pore channels, *Sci. Rep.*, 2016, **6**, 31670.

44 T. Tsuji, K. Kozai, H. Ishino and S. Kawano, Direct observations of thermophoresis in microfluidic systems, *Micro Nano Lett.*, 2017, **12**, 520–525.

45 T. Tsuji, S. Saita and S. Kawano, Dynamic pattern formation of microparticles in a uniform flow by an on-chip thermophoretic separation device, *Phys. Rev. Appl.*, 2018, **9**, 024035.

46 T. Tsuji, Y. Sasai and S. Kawano, Thermophoretic manipulation of micro-and nanoparticle flow through a sudden contraction in a microchannel with near-infrared laser irradiation, *Phys. Rev. Appl.*, 2018, **10**, 044005.

47 L. Lin, J. Zhang, X. Peng, Z. Wu, A. C. Coughlan, Z. Mao, M. A. Bevan and Y. Zheng, Opto-thermophoretic assembly of colloidal matter, *Sci. Adv.*, 2017, **3**, e1700458.

48 K. Setoura, T. Tsuji, S. Ito, S. Kawano and H. Miyasaka, Opto-thermophoretic separation and trapping of plasmonic nanoparticles, *Nanoscale*, 2019, **11**, 21093–21102.

49 J. Rotne and S. Prager, Variational treatment of hydrodynamic interaction in polymers, *J. Chem. Phys.*, 1969, **50**, 4831–4837.

50 H. Yamakawa, Transport properties of polymer chains in dilute solution: hydrodynamic interaction, *J. Chem. Phys.*, 1970, **53**, 436–443.

51 J. Zhang, S.-J. Huang, F.-Q. Zhu, W. Shao and M.-S. Chen, Dimensional properties of Laguerre–Gaussian vortex beams, *Appl. Opt.*, 2017, **56**, 3556–3561.

52 Y. Harada and T. Asakura, Radiation forces on a dielectric sphere in the Rayleigh scattering regime, *Opt. Commun.*, 1996, **124**, 529–541.

53 W. Qian, K. Doi and S. Kawano, Effects of polymer length and salt concentration on the transport of ssDNA in nanofluidic channels, *Biophys. J.*, 2017, **112**, 838–849.

54 T. Li, S. Kheifets, D. Medellin and M. G. Raizen, Measurement of the instantaneous velocity of a Brownian particle, *Science*, 2010, **328**, 1673–1675.

55 I. Hanasaki, Y. Kazoe and T. Kitamori, Time resolution effect on the apparent particle dynamics confined in a nanochannel evaluated by the single particle tracking subject to Brownian motion, *Microfluid. Nanofluid.*, 2018, **22**, 56.

56 K. Zahn, J. M. Méndez-Alcaraz and G. Maret, Hydrodynamic interactions may enhance the self-diffusion of colloidal particles, *Phys. Rev. Lett.*, 1997, **79**, 175.

57 J. Happel and H. Brenner, *Low Reynolds number hydrodynamics: with special applications to particulate media, Springer Science & Business Media*, 2012, vol. 1.

58 D. A. Drew, The force on a small sphere in slow viscous flow, *J. Fluid Mech.*, 1978, **88**, 393–400.